



# GASP XXIV. The History of Abruptly Quenched Galaxies in Clusters

Benedetta Vulcani<sup>1</sup>, Jacopo Fritz<sup>2</sup>, Bianca M. Poggianti<sup>1</sup>, Daniela Bettoni<sup>1</sup>, Andrea Franchetto<sup>1,3</sup>, Alessia Moretti<sup>1</sup>, Marco Gullieuszik<sup>1</sup>, Yara Jaffé<sup>4</sup>, Andrea Biviano<sup>5,6</sup>, Mario Radovich<sup>1</sup>, and Matilde Mingozzi<sup>1</sup>

<sup>1</sup>INAF-Osservatorio astronomico di Padova, Vicolo Osservatorio 5, I-35122 Padova, Italy; [benedetta.vulcani@inaf.it](mailto:benedetta.vulcani@inaf.it)

<sup>2</sup>Instituto de Radioastronomía y Astrofísica, UNAM, Campus Morelia, A.P. 3-72, C.P. 58089, Mexico

<sup>3</sup>Dipartimento di Fisica & Astronomia “Galileo Galilei,” Università di Padova, vicolo dell’ Osservatorio 3, I-35122, Padova, Italy

<sup>4</sup>Instituto de Física y Astronomía, Universidad de Valparaíso, Avda. Gran Bretaña 1111 Valparaíso, Chile

<sup>5</sup>INAF-Osservatorio Astronomico di Trieste, via G.B. Tiepolo 11, I-34143 Trieste, Italy

<sup>6</sup>IFPU-Institute for Fundamental Physics of the Universe, via Beirut 2, I-34014 Trieste, Italy

Received 2019 December 17; revised 2020 February 23; accepted 2020 March 1; published 2020 April 7

## Abstract

The study of cluster post-starburst galaxies gives useful insights on the physical processes quenching the star formation in the most massive environments. Exploiting the *Multi Unit Spectroscopic Explorer* data of the GAs Stripping Phenomena in galaxies project, we characterize the quenching history of eight local cluster galaxies that were selected for not showing emission lines in their fiber spectra. We inspect the integrated colors, the  $H\beta$  rest-frame equivalent widths (EW), star-formation histories (SFHs), and luminosity-weighted age (LWA) maps finding no signs of current star formation throughout the disks of these early-spiral/S0 galaxies. All of them have been passive for at least 20 Myr, but their SF declined on different timescales. In most of them, the outskirts reached undetectable SFRs before the inner regions (“outside-in quenching”). Our sample includes three post-star-forming galaxies, two passive galaxies, and three galaxies with intermediate properties. The first population shows blue colors, deep  $H\beta$  in absorption ( $EW \gg 2.8 \text{ \AA}$ ), young ages ( $8.8 < \log(\text{LWA (yr)}) < 9.2$ ). Two of these galaxies show signs of a central SF enhancement before quenching. Passive galaxies have instead red colors,  $EW(H\beta) < 2.8 \text{ \AA}$ , ages in the range  $9.2 < \log(\text{LWA (yr)}) < 10$ . Finally, the other galaxies are most likely in transition between a post-star-forming and passive phase, as they quenched in an intermediate epoch and have not lost all of the star-forming features yet. The outside-in quenching, the morphology, and kinematics of the stellar component, along with the position of these galaxies within massive clusters ( $\sigma_{\text{cl}} = 550\text{--}950 \text{ km s}^{-1}$ ) point to a scenario in which ram pressure stripping has removed the gas, leading to quenching. Only the three most massive galaxies might alternatively have entered the clusters already quenched. These galaxies are therefore at the final stage of the rapid evolution galaxies undergo when they enter the cluster environment.

*Unified Astronomy Thesaurus concepts:* Galaxy formation (595); Galaxy clusters (584); Galaxy evolution (594); E+A galaxies (424); Galaxies (573); Star formation (1569)

## 1. Introduction

During its life, a galaxy moves from the star-forming blue cloud to the quiescent red sequence through a number of different pathways (Barro et al. 2014; Schawinski et al. 2014; Vulcani et al. 2015). The cessation of star formation can take place on different timescales, strongly dependent on a galaxy’s growth history (Martin et al. 2007) and on galaxy environment (Balogh et al. 2004).

Galaxy clusters are relatively hostile environments where the impact of environmental quenching should reveal itself most prominently. Many physical mechanisms may act in clusters to both trigger and truncate star formation in infalling galaxies (see Boselli & Gavazzi 2006, for a review). The processes can be divided into two categories: interactions between the galaxy gas and the hot ( $10^7\text{--}10^8 \text{ K}$ ), rarefied ( $10^{-3} \text{ particles cm}^{-3}$ ) intracluster medium (ICM), and gravitational interactions either between the galaxy with other cluster members or with the cluster’s gravitational potential.

Ram pressure and viscous stripping (Gunn & Gott 1972; Nulsen 1982) are hydrodynamical interactions that fall into the first category. They can easily remove the hot gas halo reservoir, thereby leading to a gradual decline in star formation (strangulation, Larson et al. 1980; Bekki et al. 2002; Bekki 2009), almost without affecting the structure of the old stellar population. Strong ram pressure stripping can also

remove the cold disk gas that fuels star formation, leading to a possible temporal enhancement of the star formation (e.g., Vulcani et al. 2018b) and to its quenching on short timescales (Boselli et al. 2006, 2014, 2016; Roediger & Brügggen 2006; Bekki 2014; Lee et al. 2017; Fossati et al. 2018). Numerical simulations have shown that the truncation of star formation (i.e., the quenching) after ram pressure stripping can proceed outside-in (e.g., Kronberger et al. 2008; Bekki 2009, 2014), that is, galaxy outskirts reach undetectable star-formation levels before the inner regions. Gravitational interactions include tides due to the cluster potential, other galaxies, or the combined effect (harassment, Moore et al. 1996). These processes can disrupt both the distribution of old stars and the gas in a cluster galaxy, entailing transformations in the morphological, kinematical, star formation, and active galactic nucleus (AGN) properties of cluster galaxies (Byrd & Valtonen 1990; Bekki 1999). Galaxy–galaxy mergers are less frequent in the cluster cores because of the high relative velocities of the galaxies (Ghigna et al. 1998). Nonetheless, almost half of the galaxies in massive clusters are accreted through smaller, group-scale halos where mergers are expected to be efficient (McGee et al. 2009; De Lucia et al. 2012; Haines et al. 2018).

Each of the aforementioned processes should have a different impact on the star formation of recently accreted galaxies and to act on different timescales to shut off star formation.

Post-starburst (PSB) galaxies are a peculiar class of objects caught in the midst of a rapid transition from star forming to quiescent. PSBs are currently quenched, as indicated by their lack of significant nebular emission lines. Their spectra are characterized by strong Balmer absorption lines that reveal a substantial population of A stars, an indication that these galaxies have experienced either a “normal” star-formation activity, or (in the cases with the strongest lines) a burst of star formation sometime in the past 1–1.5 Gyr (Dressler & Gunn 1983; Couch & Sharples 1987; Poggianti et al. 1999). The spectra also show signs of the presence of K-giant (older) stars that dominate early-type (E) galaxy spectra. Such decomposition is at the origin of the names “ $k + a/a + k$ ,” and “ $E + A$ ,” often used to describe PSB galaxies. Given the known lifetime of A-type stars, the evolution of this population can be used as a quenching clock.

In the literature, the term PSB is generally used not only to refer to galaxies that indeed had a burst before the recent quenching but also to indicate both galaxies that simply had a rapid truncation of the star formation, without having a burst and galaxies that had an abrupt reduction of the star formation, but that still show some ongoing activity (e.g., Alatalo et al. 2016). To describe the second and third subpopulations, terms like post-star-forming and low-level, star-forming galaxies would be more appropriate. To avoid confusion, we will use the term PSB when referring to the literature results where the selection is ambiguous,  $a + k/k + a$  when discussing our own results.

Some PSBs are found in the “green valley” (e.g., Caldwell et al. 1996; Zabludoff et al. 1996; Norton et al. 2001; Pracy et al. 2009; Wong et al. 2012; Zwaan et al. 2013; Wu et al. 2014; Yesuf et al. 2014; Vulcani et al. 2015; Patarakijwanich et al. 2016; Paccagnella et al. 2017, 2019) of the optical color-magnitude diagram, indicating stellar populations will redden and evolve passively onto the red sequence, others are part of the blue cloud, or, in the most evolved cases, even the red sequence. PSB morphologies (Poggianti et al. 1999; Yang et al. 2004, 2008; Poggianti et al. 2009) and spatially resolved kinematics (Norton et al. 2001; Swinbank et al. 2012) are also consistent with late-type galaxies evolving into early-type galaxies.

Many evolutionary channels to quench PSB galaxies have been proposed, to account for the diversity of galaxy properties (e.g., Pawlik et al. 2019). Two broad scenarios can explain the formation of PSBs in different environments. The presence of PSBs in clusters, where Dressler & Gunn (1982) first observed them, is commonly believed to be due to ram pressure stripping. Gas-rich star-forming galaxies fall into clusters and their gas is removed by the interaction with the ICM, suddenly quenching their star formation (Dressler & Gunn 1982; Couch & Sharples 1987; Dressler & Gunn 1992; Poggianti et al. 1999; Balogh et al. 2000; Tran et al. 2003, 2004, 2007; Poggianti et al. 2009; Paccagnella et al. 2017). In this traditional scenario, as stellar morphologies are not affected by ram pressure stripping, the resulting PSB galaxies still resemble disk galaxies, at least until the effects of the past star formation fade away leaving an S0 galaxy (Bekki et al. 2002). This interpretation holds also for PSB galaxies in massive groups, where ram pressure is still effective (e.g., Poggianti et al. 2009; Paccagnella et al. 2019). In some cases, cluster mechanisms may quench galaxies without triggering any significant burst of star formation (Socolovsky et al. 2018).

In the field, PSB galaxies show disturbed kinematics and tidal features indicative of violent relaxation due to major, late-stage mergers (Zabludoff et al. 1996; Blake et al. 2004; Yang et al. 2004; Tran et al. 2004; Goto 2005; Yang et al. 2008; Pracy et al. 2009; French et al. 2016). Merger-induced supernova or AGN feedback can also aid in the expulsion of the gas that becomes too hot to collapse further or is expelled altogether (Sanders et al. 1988; Hopkins et al. 2006). This merger scenario is also supported by the detection of Balmer gradients and young stellar populations centrally concentrated with respect to the old population (Norton et al. 2001; Pracy et al. 2012, 2013—but see Yagi & Goto 2006; Chilingarian et al. 2009; Pracy et al. 2009; Swinbank et al. 2012 who failed to recover such trends). Moreover, field PSBs show a range of angular momentum properties, consistent with a variety of possible merger histories (Pracy et al. 2009, 2013; Swinbank et al. 2012).

Intriguingly, field PSBs have been found to hold large molecular (French et al. 2015; Rowlands et al. 2015) and cold (Zwaan et al. 2013) gas reservoirs, ruling out complete gas consumption, expulsion or starvation as the primary mechanism that ends the star formation. Significant gas reservoirs in PSB galaxies have also been predicted by simulations (Davis et al. 2019), who found that a variety of gas consumption/loss processes are responsible for the rapid evolution of this population, including mergers and environmental effects, while AGNs play only a secondary role. No observations of molecular gas of cluster PSBs are available to date.

In this context, the advent of integral field spectroscopy (IFS) is extremely useful to characterize the spatial distribution of the stellar populations and obtain information about the mechanism responsible of the PSB features. First, studies focused on a few tens of PSBs, and in most cases, only the central regions of galaxies have been observed (Chilingarian et al. 2009; Pracy et al. 2009; Swinbank et al. 2012; Pracy et al. 2012, 2013).

With the advent of large IFU spectroscopic surveys, more detailed analyses have been performed. Chen et al. (2019) analyzed 360 galaxies with either central PSB regions, or with off-center ring-like PSB regions in the Mapping Nearby Galaxies at APO (MaNGA; Bundy et al. 2015) survey. They showed that these galaxies are not simply different evolutionary stages of the same event, but rather, the former are caused by a significant disruptive event that produced a rapid decline of star formation in the central region, while the latter are caused by disruption of gas fueling to the outer regions.

Other IFS studies did not target specifically PSBs but managed to characterize PSB features in star-forming galaxies (e.g., Gullieuszik et al. 2017; Poggianti et al. 2017, 2019). Roche et al. (2015) investigated a merging system in the Calar Alto Legacy Integral Field Area (Sánchez et al. 2006) survey and found that much of the galaxy, especially the outer tidal arms, has a PSB spectrum, which is evidence of a more extensive recent episode of star formation, triggered by the previous perigalacticon passage. Rowlands et al. (2018) have used data from MaNGA to derive star-formation histories (SFHs) of different galaxy subpopulations finding that PSB regions are more common outside of the galaxy center, are preferentially found in asymmetric galaxies, and have lower gas-phase metallicity than other regions, consistent with interactions triggering starbursts and driving low-metallicity gas into regions at  $<1.5$  effective radii. Owers et al. (2019) used the Sydney–AAO Multiobject Integral

field spectrograph Galaxy Survey (Bryant et al. 2015) data to characterize the rare ( $\sim 2\%$  of galaxies with  $\log(M_*/M_\odot) > 10$ ) population of galaxies showing PSB features in more than 10% of their spectra. These galaxies are more frequent in clusters than in the low-density environments, representing 15% and 2% of non-passive galaxies, respectively. In clusters, PSB regions are confined to the galaxy external regions, while the centers are still star-forming. Conversely, in low-density environments the PSB signal is spread across the galaxies. The Owers et al. (2019) study is the only one explicitly focused on cluster galaxies.<sup>7</sup> Also based on the analysis of the location of these galaxies within their clusters, they concluded that the galaxies recently entered the clusters and are currently being quenched by ram pressure stripping.

This paper presents the characterization of the stellar properties of eight cluster galaxies targeted by the GAS Stripping Phenomena in galaxies with *Multi Unit Spectroscopic Explorer* (*MUSE*; GASP,<sup>8</sup> Poggianti et al. 2017, Paper I) survey, an ESO Large program aimed at characterizing where, how, and why gas can get removed from galaxies. These galaxies were chosen to show passive or PSB features in their fiber spectra (Paccagnella et al. 2017). Their selection was performed using the equivalent width of the  $H\delta$ . Thanks to the extremely high quality of the data obtained with the integral field spectrograph *MUSE*, we can investigate the quenching history of these galaxies. We note, however, that the *MUSE* wavelength coverage does not allow to observe  $H\delta$  at  $z \sim 0.06$ ; therefore, our analysis will be instead based on  $H\beta$ .

The galaxies presented in this paper were included in the GASP survey as galaxies at the final stage of their evolution. By construction, GASP allows us to study galaxies in various stages of ram pressure stripping (Jaffé et al. 2018, GASP IX), from pre-stripping (undisturbed galaxies, e.g., Vulcani et al. 2018b—GASP XIV, Vulcani et al. 2019—GASP XX), to initial stripping, peak stripping (Bellhouse et al. 2017—GASP II, Bellhouse et al. 2019 - GASP XV, Gullieuszik et al. 2017—GASP IV, Paper I, Moretti et al. 2018—GASP V, George et al. 2018—GASP XI, George et al. 2019—GASP XVII), and post-stripping (Fritz et al. 2017, GASP III), passive and devoid of gas (e.g., Vulcani et al. 2018a, GASP XIV).

We adopt a Chabrier (2003) initial mass function (IMF) in the mass range  $0.1\text{--}100 M_\odot$ , and the cosmological constants  $\Omega_m = 0.3$ ,  $\Omega_\Lambda = 0.7$  and  $H_0 = 70 \text{ km s}^{-1} \text{ Mpc}^{-1}$ .

## 2. The Sample

The eight GASP galaxies analyzed in this work were selected from the OMEGAWINGS survey (Gullieuszik et al. 2015). According to their fiber spectra (diameter  $2''16$ ) obtained with an AAOmega@AAT spectroscopic campaign (Moretti et al. 2017), six of these galaxies presented  $a + k/k + a$  spectra, while two had  $k$  features (Paccagnella et al. 2017). Specifically, all have no emission lines, but the former display a combination of signatures typical of both K- and A-type stars with strong  $H\delta$  in absorption ( $\text{EW}(H\delta) > 3 \text{ \AA}$ ) - indicative of post- starburst/post-star-forming galaxies whose star formation was suddenly truncated at some point during the last  $0.5\text{--}1 \text{ Gyr}$ , while the latter have weak  $H\delta$  in absorption

( $\text{EW}(H\delta) < 3 \text{ \AA}$ ) and present spectra resembling those of K-type stars, normally found in passively evolving elliptical galaxies.

Given the lack of ionized gas (see below), it is not possible to assess the presence of an AGN using the standard diagnostic diagrams (Baldwin et al. 1981). Also a search into the XMM and *Chandra* archives did not retrieve any bright source ( $L_X > 10^{42} \text{ erg s}^{-1}$ ) within  $5''$  from the galaxy centers. Nonetheless, in the very unlikely case that an AGN is present, it must be a very low-luminosity one. For example, Gonzalez-Martin et al. (2006, 2009) detected LINER-like emission due to AGN activity in objects with X-ray luminosities in the range  $1^{38}\text{--}1^{42} \text{ erg s}^{-1}$ . Therefore, it should not be the main contributor to the removal of gas (Davis et al. 2019).

The whole OMEGAWINGS parent sample of PSB galaxies is characterized in detail in Paccagnella et al. (2017, 2019).

Figure 1 compares the integrated properties of our galaxies to those discussed in Paccagnella et al. (2017). The determination of such properties is deferred to Section 3. The eight galaxies span the absolute magnitude range  $-20 < M_V < -18$  and the mass range  $8.5 < \log(M_*/M_\odot) < 10.4$ . They are therefore located in the central part of the distributions of the entire OMEGAWINGS population. The Kolmogorov–Smirnov tests detects differences only when comparing the magnitude distribution (statistic = 0.99,  $p$ -value =  $5e-08$ ), while in the other cases, distributions are indistinguishable ( $p$ -value  $> 0.3$ ). The color–magnitude diagram reveals that all of the galaxies are quite close to the border between the red and blue population ( $(B - V)_{rf} = -0.045 \times V - 0.035$ , Paccagnella et al. 2017), highlighting the transitioning phase of this class of objects. More specifically, three galaxies are already red, three are still blue, and two are in the green valley. It is interesting to note that one of those previously selected as  $k$  galaxy is still on the blue side. The morphological analysis reveals that two galaxies (one  $k$  and one  $k + a$ ) are S0s, while the rest are early spirals. For two galaxies, the morphologies could not be determined. Morphologies were derived with MORPHOT (Fasano et al. 2012), an automatic tool designed to reproduce as closely as possible the visual classifications.

The properties of the galaxies discussed in this paper are therefore consistent with the general cluster PSB population and can be considered as representative of it. Their analysis could therefore improve our understanding of the galaxy quenching mechanisms in clusters.

## 3. Methods and Observations

The galaxies were observed in service mode using the *MUSE* spectrograph mounted on the Very Large Telescope in Paranal. A complete description of the survey strategy, observations, data reduction and analysis procedure is presented in Paper I.

Most of the analysis presented in this paper is based on the outputs of our spectrophotometric code SINOPSIS (Paper III). This code searches the combination of Single Stellar Population (SSP) model spectra that best fits the equivalent widths of the main lines in absorption and emission and the continuum at various wavelengths, minimizing the  $\chi = 1$  using an adaptive simulated annealing algorithm (Fritz et al. 2007, 2011). The star-formation history is let free with no analytic priors. SINOPSIS uses a Chabrier (2003) IMF with stellar masses in the  $0.1\text{--}100 M_\odot$  limits, and they cover metallicity values from  $Z = 0.0001$  to  $0.04$ . The metallicity of the best-fit models is constant and homogeneous (i.e., all of

<sup>7</sup> The Pracy et al. (2009, 2013) samples did include two and one cluster galaxies in their sample, but did not discuss the role of their environments on shaping their properties.

<sup>8</sup> <http://web.oapd.inaf.it/gasp/index.html>

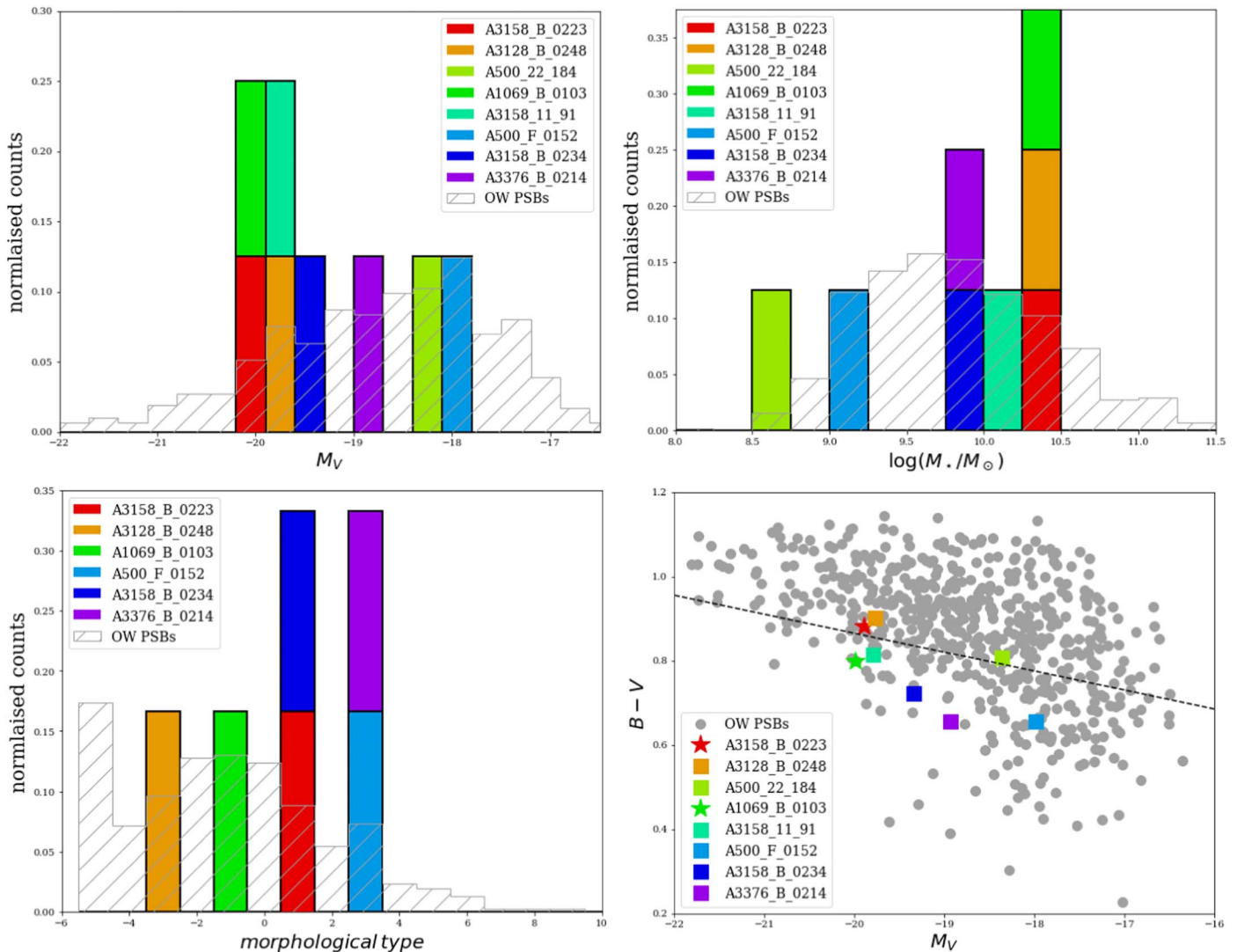


**Figure 1.** Absolute  $V$  magnitude, stellar mass, morphological distribution, and color–magnitude plot of the galaxies discussed in this paper (colored histograms and points), compared to the results presented in Paccagnella et al. (2017; OW = OMEGAWINGS, light gray histograms and points). In the color–magnitude plot,  $k$  galaxies are represented by stars,  $k + a/a + k$  galaxies by squares. Galaxies are rainbow-colored by increasing  $\text{EW}(\text{H}\beta)$ , as measured on the integrated spectra (see Table 2). The same color scheme will be adopted throughout the paper.

the SSPs have the same metallicity independently of age). The best-fit model is searched using SSP models at three different metallicity values (sub-solar, solar and super-solar). Dust extinction is accounted for by adopting the Galaxy extinction curve (Cardelli et al. 1989). SINOPSIS uses the latest SSP models from S. Charlot & G. Bruzual (2020, in preparation) based on stellar evolutionary tracks from Bressan et al. (2012) and stellar atmosphere spectra from a compilation of different authors, depending on the wavelength range, stellar luminosity, and effective temperature. SINOPSIS also includes the nebular emission lines for the young (i.e., age  $< 2 \times 10^7$  yr) SSPs computed with the Cloudy code (Ferland et al. 2013). The code provides for each *MUSE* spaxel rest-frame magnitudes, stellar masses, luminosity-weighted and mass-weighted ages, and SFHs in 12 fine age bins. These bins have also been combined in four logarithmically spaced age bins in such a way that the differences between the spectral characteristics of the stellar populations are maximal (Paper III). We consider as reliable only spaxels with  $S/N > 3$  across the entire spectrum.

Equivalent widths (EW) were measured using SPLAT,<sup>9</sup> a publicly available graphical tool. Observed EWs are converted to rest-frame values dividing the measurements by  $(1 + z)$ . We adopt the usual convention of identifying absorption lines with positive values. As explained later, EWs were measured only on spectra integrated across portions of galaxies, to reduce the noise.

Total masses are obtained by summing the values of stellar mass obtained from SINOPSIS on the single spaxels belonging to the galaxy, i.e., the region containing the spaxels whose near- $\text{H}\alpha$  continuum flux is  $\sim 1\sigma$  above the background level (as in Vulcani et al. 2018b).

We will also discuss the properties of the stellar component. The stellar kinematics were derived from the analysis of the characteristics of absorption lines, using the pPXF software (Cappellari & Emsellem 2004), which works in Voronoi binned regions of given a signal-to-noise ratio ( $S/N$ ; 10 in this case; see Cappellari & Copin 2003). The value of the stellar

<sup>9</sup> <http://star-www.dur.ac.uk/~pdraper/splat/splat.html>

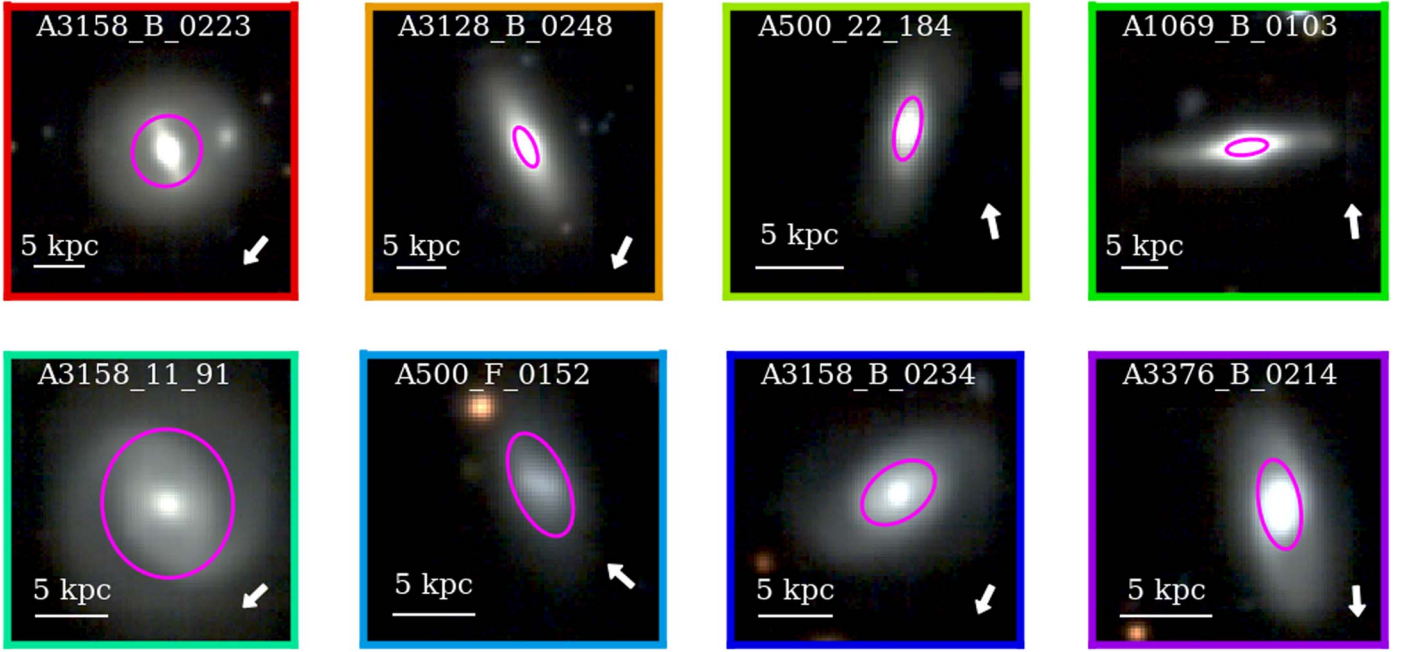


**Figure 2.** RGB images of the galaxies used in this paper, sorted by increasing stellar mass. The reconstructed  $g$ ,  $r$ ,  $i$  filters from the *MUSE* cube have been used. North is up, and east is left. Magenta ellipses show the effective radius of the galaxies. The black arrows in the lower right corners show the direction of the cluster center. Galaxies are rainbow-colored by increasing  $\text{EW}(\text{H}\beta)$ , as measured on the integrated spectra (see Table 2).

**Table 1**

Galaxy Name, Coordinates, Redshift, Stellar Mass, Cluster, Inclination, Effective Radius, Ellipticity, Position Angle, Spectral Type According to the Fiber OmegaWINGS Spectrum, and Morphology of the Sample Analyzed in the Paper

Id	R.A. (J2000)	Decl. (J2000)	$z$	Mass ( $10^9 M_\odot$ )	Cluster	$i$ (deg)	$r_e$ ( $''$ )	$\epsilon$	PA (deg)	TYPE	$T_M$
A3158_B_0223	03:41:59.80	-53:28:04.240	0.05621	23.4	A3158	20	$3.2_{-0.1}^{+0.1}$	$0.05 \pm 0.06$	150	$k$	S
A3128_B_0248	03:29:23.42	-52:26:02.871	0.05302	19.3	A3128	67	$1.9_{-0.1}^{+0.1}$	$0.59 \pm 0.02$	24	$k + a$	S0
A500_22_184	04:38:46.41	-22:13:22.368	0.07248	0.34	A500	67	$1.4_{-0.1}^{+0.1}$	$0.60 \pm 0.03$	169	$a + k$	?
A1069_B_0103	10:39:36.49	-08:56:34.822	0.06348	22.5	A1069	70	$1.8_{-0.2}^{+0.1}$	$0.64 \pm 0.04$	98	$k$	S0
A3158_11_91	03:41:16.75	-53:24:00.580	0.06135	13.9	A3158	29	$4.6_{-0.3}^{+0.3}$	$0.12 \pm 0.04$	4	$a + k$	?
A500_F_0152	04:38:21.25	-22:13:02.197	0.06951	1.4	A500	61	$2.6_{-0.3}^{+0.3}$	$0.50 \pm 0.04$	23	$a + k$	S
A3158_B_0234	03:42:24.68	-53:29:25.989	0.06602	7.1	A3158	50	$2.5_{-0.1}^{+0.1}$	$0.35 \pm 0.05$	126	$a + k$	S
A3376_B_0214	06:00:43.18	-39:56:41.641	0.04728	7.7	A3376	64	$2.8_{-0.1}^{+0.1}$	$0.54 \pm 0.01$	10	$k + a$	S

radial velocity was further smoothed using the two-dimensional local regression techniques (LOESS) as implemented in the Python code developed by M. Cappellari.<sup>10</sup>

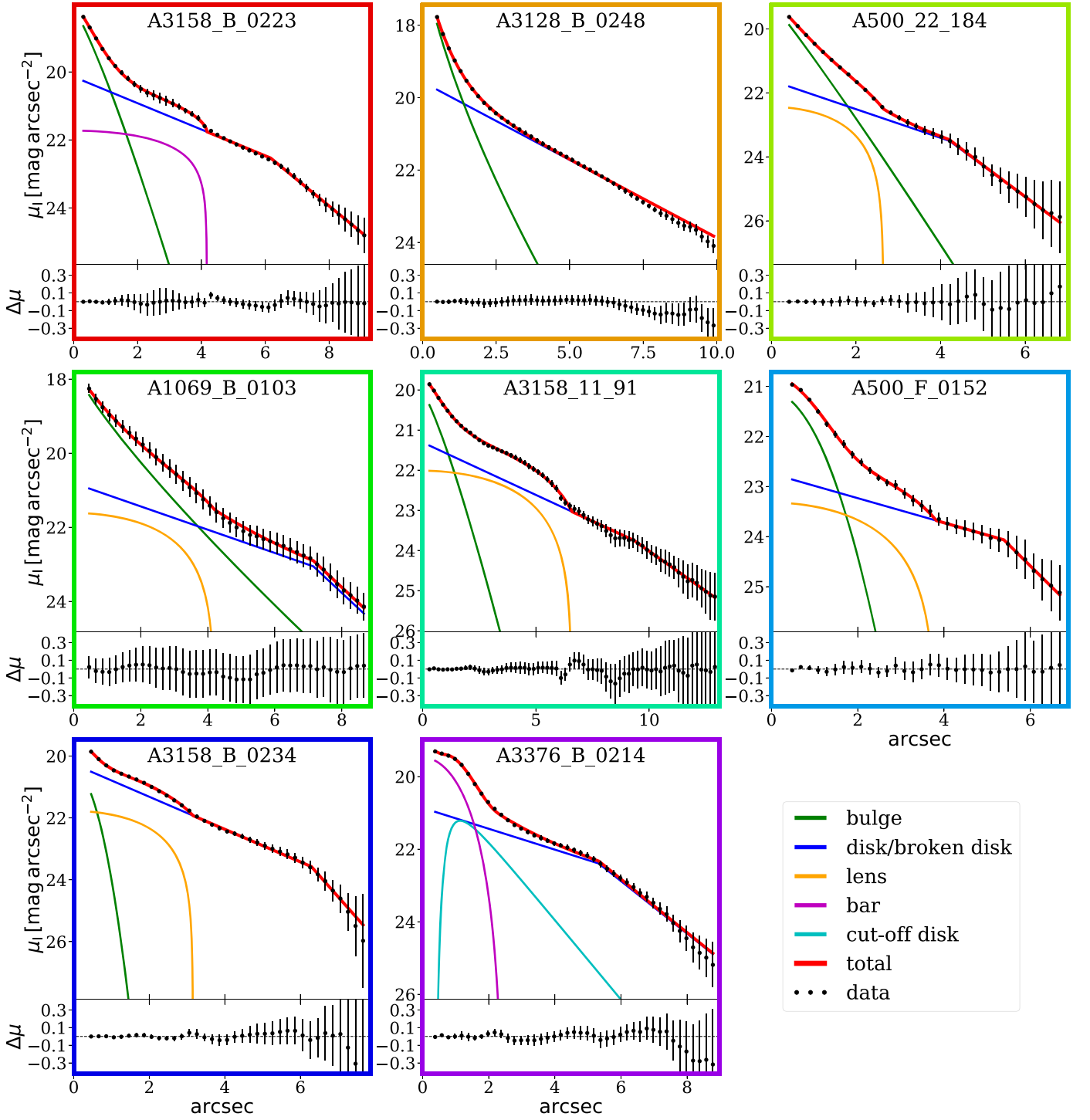
The structural parameters of the galaxies (effective radius  $R_e$ , ellipticity  $\epsilon$ , position angle  $PA$ , and inclination  $i$ ) were obtained from the analysis of the images achieved from the integrated *MUSE* data cubes, using the Cousins  $I$ -band filter response curve, as explained in Franchetto et al. (submitted). Briefly, they were obtained using the ELLIPSE task (Jedrzejewski 1987) of the software IRAF. We measured the radius of an ellipse including half of the total light of the galaxies. Then, from the surface brightness profile, we selected the isophotes that trace the stellar disk to measure their mean  $PA$ ,  $\epsilon$  and corresponding errors.  $i$  is derived from the apparent flattening assuming an intrinsic axis ratio of 0.15 and will be also used to deproject galaxy properties when studying galaxy gradients (Section 5 and 6).

Table 1 presents some properties of the targets, which will be discussed throughout in the rest of the paper. Spectral types are based on fiber spectra (Paccagnella et al. 2017). It is interesting to note that the two  $k$  galaxies are also the most massive ones of the sample. In the following, we will provide a new classification scheme, based on the spatially resolved properties of the galaxies.

#### 4. Galaxy Morphologies

Figure 2 shows the galaxy images based on the reconstructed  $g$ ,  $r$ ,  $i$  filters from the *MUSE* cube. Each galaxy is surrounded by a color that will be used throughout the paper to identify galaxies. This Figure shows that galaxies present either an early spiral or an S0 morphology, with both bulges and disks clearly distinguishable. Galaxies are also characterized by a wide range of inclinations, going from 30 to 70 degrees. They do not present evident signs of interaction with companions. The object visible on the northwest side of A3158\_B\_0223 is a background passive galaxy ( $z = 0.064$ ). Since the object has no emission lines, its presence does not affect the forthcoming

<sup>10</sup> <http://www-astro.physics.ox.ac.uk/~mxc/software>

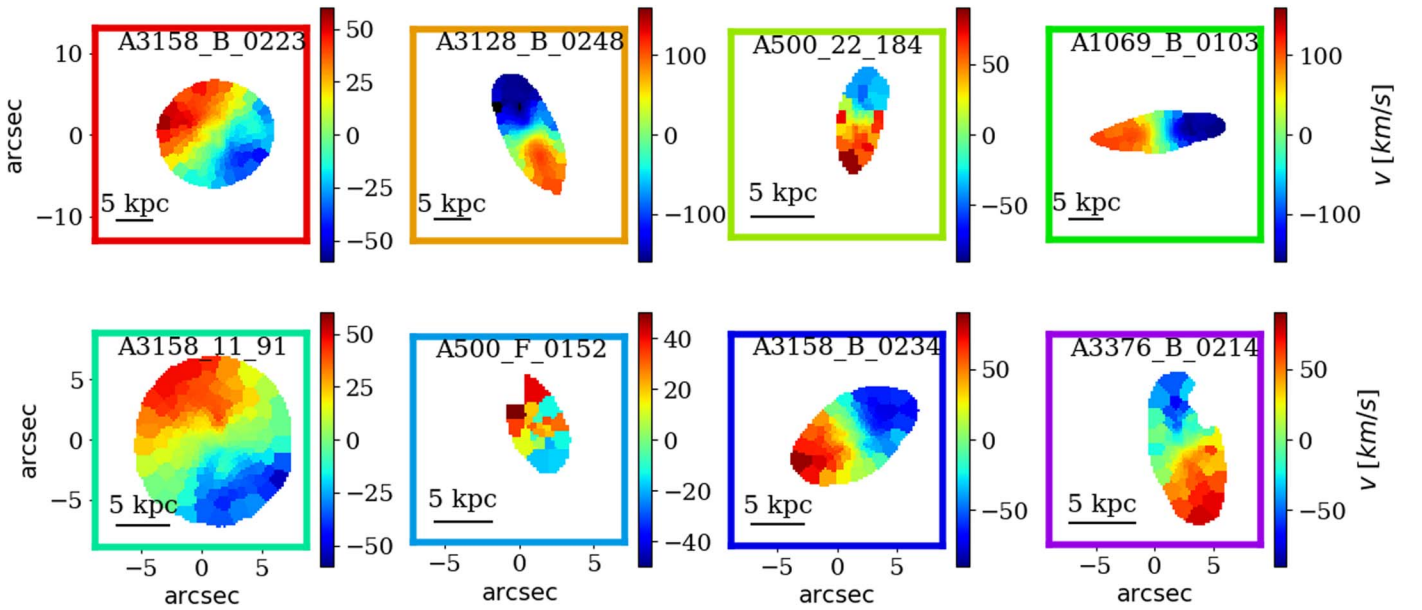


**Figure 3.** Surface brightness profiles and errors as derived from the  $I$  band images of the eight galaxies, sorted by increasing stellar mass. For each galaxy, the main panel shows the decomposition, the bottom panel the residual of the data with respect to the fit. Black points with errors are the data, the red lines represent the estimated surface brightness profile. The different components used to decompose the galaxies are represented with different colors, as indicated in the labels. Galaxies are rainbow-colored by increasing  $\text{EW}(\text{H}\beta)$ , as measured on the integrated spectra (see Table 2).

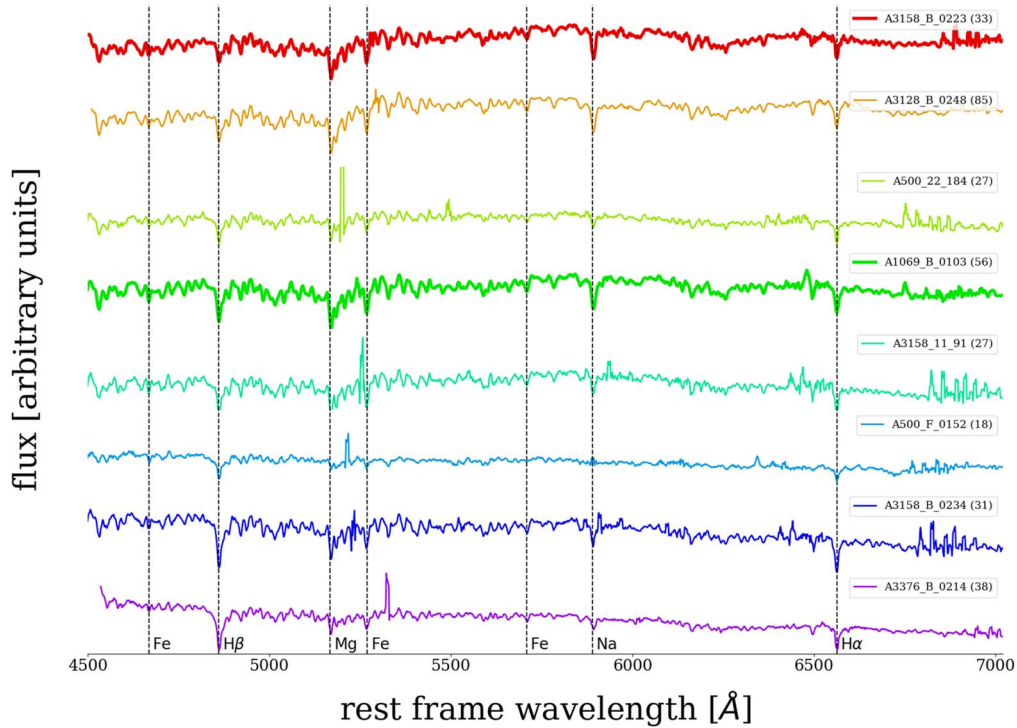
results, and it will not be masked. A3376\_B\_0214 also contains two background galaxies toward the northwest. These galaxies are star forming, at a redshift of 0.7596, and they will be masked in the forthcoming analysis.

Figure 3 shows the photometric decomposition of the galaxies, performed on the  $I$  band *MUSE* images. Details on the procedure adopted to obtain the parameters of the different components are

given in Franchetto et al. (2020, in preparation) and in the Appendix. The Figure unveils that galaxies are composed by many subcomponents. All galaxies but A3376\_B\_0214 are characterized by the presence of a nonnegligible bulge, whose size ranges from  $1''$  to  $8''$  at  $\mu_l = 25 \text{ mag arcsec}^{-2}$ . Only A3128\_B\_0248 can be decomposed just in terms of a bulge and a disk, while all of the other galaxies present a more complex



**Figure 4.** Stellar velocity map for Voronoi bins with  $S/N > 10$  of the eight galaxies. The stellar radial velocities were further smoothed using two-dimensional local regression techniques (LOESS). Galaxies are surrounded by squares that are colored following the scheme of Figure 1. Galaxies are rainbow-colored by increasing  $EW(H\beta)$ , as measured on the integrated spectra (see Table 2).



**Figure 5.** Integrated spectrum of the galaxies in the sample. Spectra are arbitrarily shifted for display purposes. Galaxies represented by thicker lines have  $k$  fiber spectra. Numbers in parenthesis are the mean  $S/N$  ratio as measured on the entire integrated spectrum. Galaxies are rainbow-colored by increasing  $EW(H\beta)$ , as measured on the integrated spectra (see Table 2).

structure that includes either a bar or a lens and are characterized by a broken disk (Type II).

This finding might suggest that bars and other internal structures may play a significant role in triggering bursts of star formation in these galaxies or, vice versa, that during the quenching process or the SF enhancement prior to it, a bar or another structure is formed.

No signs of interactions are evident from Figure 4, which shows the stellar velocity map of the galaxies. Galaxies present

a rather undisturbed morphology and kinematics and regular rotation. Some distortions are evident in A3158\_11\_91 and A3376\_B\_0214 but these are most likely due to the presence of bars and lenses. Stellar velocity dispersions are also generally quite low ( $< 50 \text{ km s}^{-1}$ , plots not shown).

In what follows, when measuring gradients, we will not take into account the galaxy internal structure, but it will be important to keep in mind the coexistence of different components.

**Table 2**  
Rest-frame  $EW(H\beta)$  Measured on the Integrated Spectra

Id	$EW(H\beta)$ (Å)
A3158_B_0223	$2.28 \pm 0.05$
A3128_B_0248	$2.65 \pm 0.06$
A500_22_184	$3.10 \pm 0.05$
A1069_B_0103	$3.12 \pm 0.04$
A3158_11_91	$3.12 \pm 0.04$
A500_F_0152	$3.74 \pm 0.04$
A3158_B_0234	$4.38 \pm 0.05$
A3376_B_0214	$5.25 \pm 0.07$

## 5. Equivalent Width of Absorption Lines

Figure 5 shows the integrated spectra obtained from *MUSE*. Galaxies show no emission lines and, therefore, ionized gas, demonstrating that there is no significant level of star formation throughout the whole galaxy and not only in the regions probed by the fiber spectra (Paccagnella et al. 2017). Figure 5 also highlights how all galaxies show deep  $H\beta$  in absorption, as well as a number of other lines. Unfortunately, the *MUSE* wavelength coverage does not allow us to sample the  $H\delta$  line, upon which most of the PSB analysis in the literature relies. In what follows, we will therefore characterize the  $H\beta$  instead. Table 2 gives the values of the rest-frame  $EW(H\beta)$  for the galaxies, measured on the integrated spectrum. Values are the average of 10 measurements, obtained by independently shifting each time the continuum bands of few Å and the  $H\beta$  band of few tenths of Å. Reported uncertainties are the standard errors on the means.

To put these numbers in context, we have measured the  $EW(H\beta)$  of a set of model spectra. These spectra were built from the same set of SSP models used in SINOPSIS (see Section 3), and using a solar metallicity value, assuming a two-parameters analytical SFH, represented by a log-normal distribution (Gladders et al. 2013):

$$SFR(t) = \frac{1}{t\tau\sqrt{2\pi}} \cdot \exp\left[-\frac{(\ln t - t_0)^2}{2\tau^2}\right] \quad (1)$$

where  $t$  is the time in yr since the big bang,  $t_0$  the logarithmic delay time, and  $\tau$  the parameter that sets the initial SFR timescale.

The final model spectrum is obtained by summing the SSPs of different ages, each one weighted by a given stellar-mass value calculated from the SFH. For the sake of simplicity, we did not include dust extinction. The age of the SSP goes from  $10^4$  to  $T_{\max}$ , where the latter is calculated based on the age of the universe at the model’s redshift, and assuming a galaxy formation redshift of 20. We choose a model redshift of 0.06, similar to that of the galaxies in the sample, which gives  $T_{\max} = 12.25$  Gyr in the adopted cosmology.

We explored model spectra obtained from a combination of the free parameters of the log-normal prescription that allows us to simulate SFH of galaxies across the whole Hubble sequence: from elliptical ( $\tau = 0.1$  and  $t_0 = 20.7$ , representing a short burst at the formation epoch), to actively star-forming spiral (e.g.,  $\tau = 1.0$  and  $t_0 = 22.1$ ). Furthermore, for each of the SFHs, we have created a similar model but applying also a truncation in the SFR at epochs of  $10^8$ ,  $5 \times 10^8$ , and  $10^9$  yr ago, to simulate a sudden quenching at different epochs. Truncation at  $10^{10}$  yr ago replicates the spectrum of elliptical

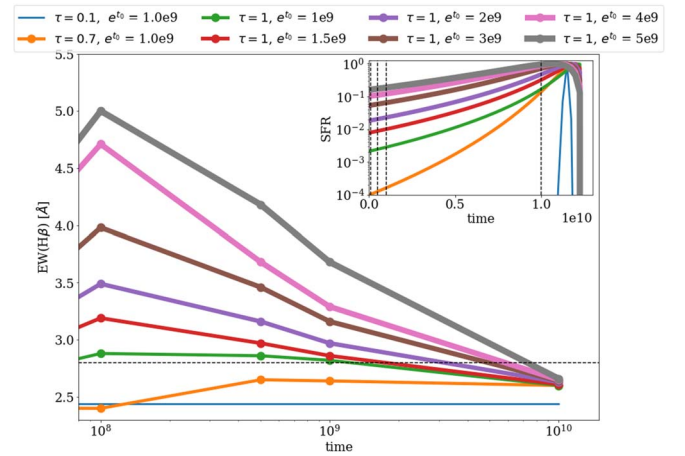


**Figure 6.**  $EW(H\beta)$  as a function of truncation time measured on a set of model spectra, obtained from a combination of the free parameters of a log-normal prescription that allows us to simulate SFH of a range of galaxies. The corresponding SFHs are shown in the inset. SFHs have been truncated at different epoch (see vertical dashed lines) to simulate a sudden quenching at different epochs (see the text for details). The horizontal dotted line shows the value adopted to separate  $k + a/a + k$  from  $k$  spectra.

galaxies. A schematic view of the different set of models along with the different parameters is presented in the legend of Figure 6.

We then measured the  $EW(H\beta)$  on the model spectra and found that SFHs representative of elliptical galaxies produce spectra with  $EW(H\beta) \sim 2.5$  Å, while SFHs representative of actively star-forming galaxies have, as expected,  $H\beta$  in emission. Spectra of star-forming galaxies whose star formation has been truncated instead have  $H\beta$  in absorption whose magnitude depends on the epoch of the truncation. Figure 6 shows that star-forming galaxies (represented by model SFHs with  $\tau = 1.0$ ) whose star formation was truncated around  $10^9$  yr ago or even more recently have always  $EW(H\beta) \geq 2.8$  Å (corresponding to the green point at  $t = 10^9$  yr in Figure 6). This value can be adopted as a lower limit to identify galaxies in a post-star-forming phase. Galaxies having a burst prior to quenching will have even larger  $EW(H\beta)$  values.

We are now in the position of interpreting the integrated  $EW$  values shown in Table 2: A3128\_B\_0248, and A3158\_B\_0223 have  $EW(H\beta)$  measured  $< 2.8$  Å, while A1069\_B\_0103, A3158\_11\_91 and A500\_22\_184 have a value slightly above the threshold. The  $EW(H\beta)$  is therefore consistent with a scenario where the star formation of the former galaxies ended more than  $\sim 10^9$  yr ago and that in the latter galaxies ended slightly earlier.

The rest of the sample is characterized by  $EW(H\beta)$  between 3.1 and 5.2 Å, consistent with populations quenched few  $10^8$  yr ago and possibly having experienced a burst prior to the truncation.

For each galaxy, we can also characterize spatial trends in  $H\beta$  as a function of the galactocentric distance. To reduce the noise, we compute EWs on stacked spectra. We consider annuli, defined as the regions in between elliptical apertures, which are chosen to match roughly the surface brightness intensity of the stellar emission at different levels. For all galaxies, we consider 10 equally spaced annuli, but for the two smallest galaxies, we consider only five annuli.

Figure 7 shows the EW as a function of the galactocentric distance, normalized by  $r_e$ . Different trends can be seen and galaxy-by-galaxy variations are observed.  $EW(H\beta)$  is

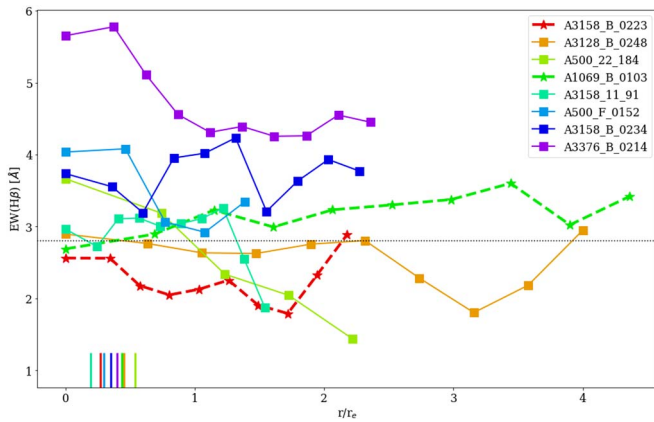


**Figure 7.** Rest-frame  $EW(H\beta)$  gradients in units of  $r_e$ , for each galaxy of the sample. A small horizontal shift has been applied to the points for display purposes. Galaxies represented by stars have  $k$  integrated spectra, galaxies represented by squares have  $k + a/a + k$  integrated spectra. The thick vertical lines on the bottom indicate the size of 1 kpc in unit of  $r_e$  for each galaxy. The horizontal dotted line shows the value adopted to separate  $k + a/a + k$  from  $k$  spectra.

lower than  $2.8 \text{ \AA}$  at all distances for A3128\_B\_0248, and A3158\_B\_0223. These galaxies are therefore truly passive at all galactocentric distances. A1069\_B\_0103 and A3158\_11\_91 have  $EW(H\beta) < 3 \text{ \AA}$  in the galaxy center, then values are slightly higher in the outskirts, but never exceed  $EW(H\beta) \sim 3.5 \text{ \AA}$ . Overall trends are rather flat. A500\_22\_184 is instead characterized by a very steep negative gradient. The  $EW(H\beta)$  is  $3.8 \text{ \AA}$  in the galaxy center and then reaches values  $< 2 \text{ \AA}$  in the outskirts. The galaxy could therefore have been passive for a longer time in the outskirts and just recently could have become quickly passive in the core or could have had experienced a recent increase in the SF within the core.

The other three galaxies have  $EW(H\beta) \gg 2.8 \text{ \AA}$  at all distances from the center. They also show higher  $EW(H\beta)$  values in the cores. A3376\_B\_0214 is the galaxy with the overall highest EW and also the highest EW in the center, with values ranging between 4.1 and  $5.9 \text{ \AA}$ , followed by A500\_F\_0152 that also shows a strong  $EW(H\beta)$  gradient. In contrast, A3158\_B\_0234 presents a flat trend.

Figure 7 also shows the size of 1 kpc in unit of  $r_e$ , a region often inspected by other studies. The results will be discussed in Section 7.

To summarize the results so far, our sample includes two galaxies (A3128\_B\_0248, A3158\_B\_0223) that have  $EW(H\beta) < 2.8 \text{ \AA}$  throughout the entire galaxy disks, indicating that they have stopped forming stars at early epochs. These galaxies are also the two reddest galaxies in the sample (see Figure 1) and are among the most massive galaxies. The sample also includes three galaxies (A500\_F\_0152, A3158\_B\_0234, and A3376\_B\_0214) whose  $EW(H\beta)$  measured on the integrated spectra is  $\gg 2.8 \text{ \AA}$ , suggesting a recent truncation of their star formation ( $< 10^9$  yr ago). Two of these galaxies have strong negative  $EW(H\beta)$  gradients, suggesting the presence of a central burst before quenching. All of these galaxies still show blue colors in Figure 1. The remaining three galaxies have  $EW(H\beta) \sim 3.1 \text{ \AA}$ . A1069\_B\_0103 and A3158\_B\_0234 have flat  $EW(H\beta)$  gradients and green colors, while A500\_22\_184 have a steep negative gradient ( $EW(H\beta) \sim 3.8 \text{ \AA}$  in the core) but redder colors. The last galaxy could therefore have been passive in the outskirts for a longer

time but could have had an abrupt truncation of the star formation in the core recently.

## 6. Spatially Resolved Properties

### 6.1. SFHs

A further characterization of the quenching process these galaxies underwent can be obtained inspecting their spatially resolved SFHs, obtained using SINOPSIS.

Figure 8 shows the variation of the SFR maps with cosmic time in four age bins. Given that no emission lines are detected, none of the galaxies have star formation in the youngest age bin (last  $2 \times 10^7$  yr), consistent with the fact that they are all truly passive today. All of the galaxies have stopped forming stars at least 20 Myr ago and were highly star-forming in the oldest age bin. In contrast, they present different characteristics in the two intermediate bins. A3376\_B\_0214 is the only galaxy showing a clear sign of a central SF enhancement between  $2.7 \times 10^7$  yr and  $5.7 \times 10^8$  yr ago. The three galaxies with the highest  $EW(H\beta)$  (A500\_F\_0152, A3158\_B\_0234 and A3376\_B\_0214) show only mild signs of star-formation truncation in the galaxy outskirts in the second age bin (between  $2.7 \times 10^7$  yr and  $5.7 \times 10^8$  yr ago) compared to the third age bin (between  $5.7 \times 10^8$  yr and  $5.7 \times 10^9$  yr ago), indicating that the bulk of the quenching process occurred more recently than  $2.7 \times 10^7$  yr ago. In contrast, the other galaxies show clearly that the quenching process started at earlier epochs and proceeded from the external regions toward the galaxy cores (outside-in quenching). The outside-in quenching is better observed in Figure 9, which shows the ratio of the number of spaxels that were star-forming in the second age bin to the number of spaxels that were star-forming in the third age bin, measured in annuli at different galactocentric distances. These are the two age bins that better capture the quenching: at older epochs, all spaxels were star-forming; in the youngest age bin, the galaxies are completely quenched. The figure shows that in the galaxy cores, all spaxels are star-forming in both age bins, while as we proceed from the galaxy cores toward the outskirts, the fraction of star-forming spaxels decreases, indicating that a larger portion of the galaxies is already quenched. A3158\_B\_0223 is the galaxy with the strongest evidence of outside-in quenching, while the trends for A328\_B\_0248 and A1069\_B\_0103 have to be taken carefully because the former galaxy is very small and so there are not many spaxels in each galactocentric distance bin and the latter has a high inclination, and annuli enclose portion of the galaxies that might be physically different.

The left panels of Figures 10 and 11, show more in detail the SFHs, both integrated over the whole galaxy disks and in different regions of the galaxies. Trends are shown with errors, which are computed as the standard deviation on the plotted median values. Uncertainties on the SFR measured on each spaxel are negligible.<sup>11</sup>

Considering integrated values, we observe that even though all galaxies are quenched today, they reached the passive state through different paths.

The two  $a + k/k + a$  galaxies with strong EW gradients (A500\_F\_0152 and A3376\_B\_0214) show an increase of the SFR in the second age bin before the quenching—suggesting again an

<sup>11</sup> Following the approach explained in Fritz et al. (2007), for each spaxel, we have run SINOPSIS 11 times for each chosen value of the SSP metallicity: the final results have been used to obtain lower and upper limits for the SFR in the different age bin. When these are binned not only temporally but also spatially to get radial profiles, we have found that the dominant source of uncertainty is the spaxel-to-spaxel variation, which we have reported in the plots. We explained this in the text.

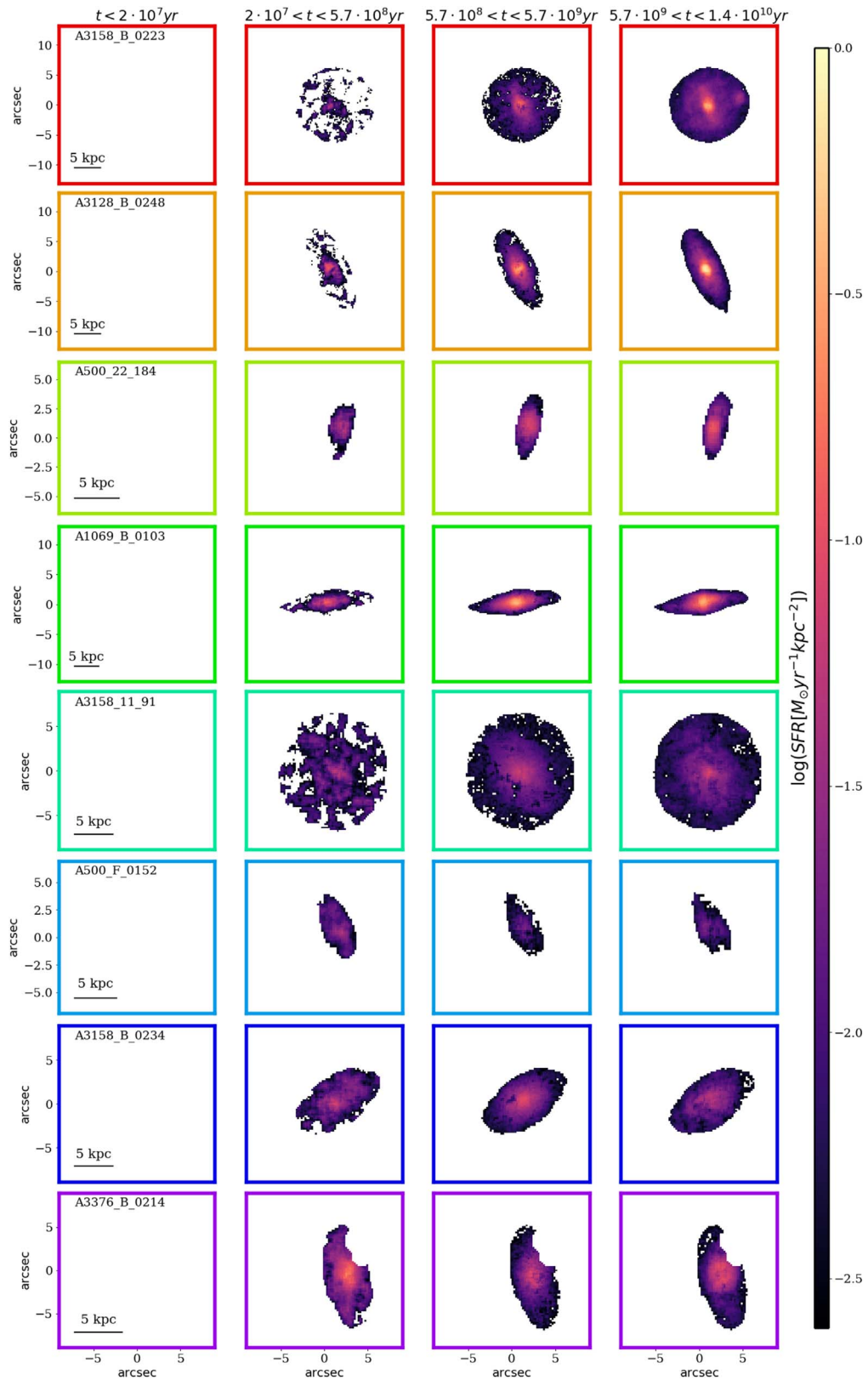


**Figure 8.** Stellar maps of different ages, illustrating the average star-formation rate per  $\text{kpc}^2$  during the last  $2 \times 10^7$  yr (left panels), between  $2 \times 10^7$  yr and  $5.7 \times 10^8$  yr (central left panels),  $5.7 \times 10^8$  yr and  $5.7 \times 10^9$  yr (central right panels), and  $>5.7 \times 10^9$  yr ago (right panels), for each galaxy, separately. Galaxies are surrounded by squares colored following the scheme of Figure 1. Galaxies are rainbow-colored by increasing  $\text{EW}(\text{H}\beta)$ , as measured on the integrated spectra (see Table 2).

enhancement before the truncation of the star formation, while A3158\_B\_0234 presents a rather flat trend. In contrast, all of the other galaxies show a steady decline of the SFR from the oldest toward the youngest ages.

Moving the attention to portions of galaxies at different galactocentric distances, we observe that, at any given epoch, the median SFR is always the highest in the core and then it decreases toward the outskirts, in a monotonic manner. This

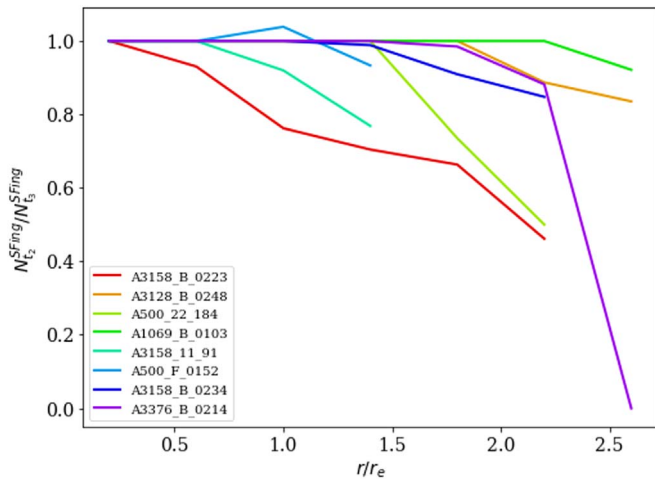


**Figure 9.** Ratio of the number of spaxels that were star forming in the second age bin ( $t_2 = 2.7 \times 10^7$  yr  $- 5.7 \times 10^8$  yr ago) to the number of spaxels that were star forming in the third age bin ( $t_3 = 5.7 \times 10^8$  yr  $- 5.7 \times 10^9$  yr ago), as a function of the galactocentric distance.

behavior is partially due to the fact that the stellar mass is concentrated to the center: if we inspect the sSFHs (plot not shown), we obtain a smaller variation with distance. The remaining scatter indicates that the galaxy outskirts have been always less effective in forming new stars.

Second, we observe that the SFHs at a given distance do not follow exactly the integrated value indicating that different portions of the galaxy assembled their mass differently. In particular, the outskirts of A3158\_11\_91, A3128\_B\_0248 and A3158\_B\_0223 became passive between  $5.7 \times 10^8$  and  $5.7 \times 10^9$  yr ago.

The right panels of Figures 10 and 11 show the luminosity-weighted age maps, which provide an estimate of the average age of the stars weighted by the light, therefore giving us an indication of when the last episode of star formation occurred. An age spread among galaxies is detected, with galaxies showing  $a + k/k + a$  spectra having systematically younger ages (between  $8.8 < \log(\text{age (yr)}) < 9.2$ ) than the other galaxies (between  $9.2 < \log(\text{age (yr)}) < 9.8$ ). No particularly strong radial variations with distance are observed. Figure 12 shows in detail the variation of the luminosity-weighted ages with distance, in units of  $r_e$ , similarly to what is shown in Figure 7 for the EW( $H\beta$ ). The Figure shows a mix of flat, positive, and negative gradients, which might suggest a mix of outside-in, inside-out, and simultaneous quenching. In particular, A3376\_B\_0214—the galaxy with the most outstanding EW( $H\beta$ ) negative gradient—presents a dip in the LWA gradient in the core, indicative of a younger age, and then a rather flat gradient. Similarly, also the other galaxies with  $a + k/k + a$  spectra and A500\_22\_184 show positive gradients, suggesting the presence of younger ages in the cores. A500\_F\_0152 shows a significant younger age at  $r/r_e < 1$  than  $r/r_e > 1$ . This is consistent with what found in Figure 7, where this galaxy showed a very steep EW( $H\beta$ ) gradient.

The other galaxies present overall flat or even negative gradients. These results are supported by the Pearson  $r$ -correlation test (see Table 3). Results of Figure 7 and Figure 12 are therefore consistent and show how the EW( $H\beta$ ) is a good age tracer.

## 7. Discussion

In this paper, we have characterized the spatially resolved properties of six galaxies showing  $k + a/a + k$  fiber (central  $\sim 2$  kpc) spectra and two having  $k$  fiber spectra. The goal is to understand their pathway to the quenching state, what are the mechanisms that affected their star-formation activity, and on what timescales.

The first important result is that galaxies are entirely quenched, and no signs of emission lines are detected throughout the galaxy disks. As these galaxies were selected on the basis of fiber spectra, it could have been that only the central regions of the galaxies were characterized by  $k + a/a + k$  features, while star-forming regions were still present in the outskirts.

We investigated the integrated properties and the spatial distribution of the stellar populations to obtain information about the mechanism responsible of the galaxy features.

The analysis of the surface brightness profiles has shown that most of the galaxies are characterized by the presence of either bars, lens, or truncated Type II disks. Head et al. (2015) have found that the bar fraction is considerably higher in galaxies hosting a Type II disk than in galaxies whose disk remains unbroken. This implies that either the truncation mechanism induces bar growth, or that bars stabilize disks during truncation, such that the detection of a disk break for bright galaxies is more likely if a bar is present. The significant increase in bar size for more luminous Type II galaxies may therefore suggest a period of enhanced star formation in the bar due to gas inflows, visible as a burst. Even regardless of the presence of a bar, truncated disks alone are also indicative of an episode of star formation that lasted longer in the galaxy center than in the outskirts: the steeper profile of the inner stellar disk is likely due to the inside-out growth mode of the disks (Elmegreen & Parravano 1994; Martinez-Serrano et al. 2009).

Central bursts and a rapid cutoff of the star formation can also leave a young stellar population in a centrally concentrated cusp (with scales of  $\sim 1$  kpc, Bekki et al. 2005; Hopkins et al. 2009) and an old stellar population distributed like a normal early-type galaxy (Hopkins et al. 2009; Snyder et al. 2011).

However, from the observational point of view, results regarding the spatial distribution of PSBs and the presence of stellar population gradients are still controversial. On one side, Norton et al. (2001), Yagi & Goto (2006), and Chilingarian et al. (2009) found evidence that the young stellar population is not confined to the galaxy core but extends over  $\sim 2-3$  kpc; likewise, Pracy et al. (2009) were unable to detect any Balmer line gradients or central concentration in the young population, and Swinbank et al. (2012) claimed that the characteristic PSB signature is a property of the galaxy as a whole and not due to a heterogeneous mixture of populations.

On the other hand, Pracy et al. (2005) and Snyder et al. (2011) did observe a Balmer line absorption enhancement and gradient in the central regions, interpreted as proxy for the existence of a young component in PSB galaxies. Pracy et al. (2013) have analyzed four low-luminosity PSBs in different environments, including a cluster member and found that all four galaxies do have centrally concentrated gradients in the young stellar population contained within the central  $\sim 1$  kpc.

In Figure 7, we have shown the  $H\beta$  gradients for our sample and highlighted the 1 kpc size for each galaxy separately. In agreement with the results presented by Pracy et al. (2013), the galaxies classified as  $k + a/a + k$  show hints of centrally

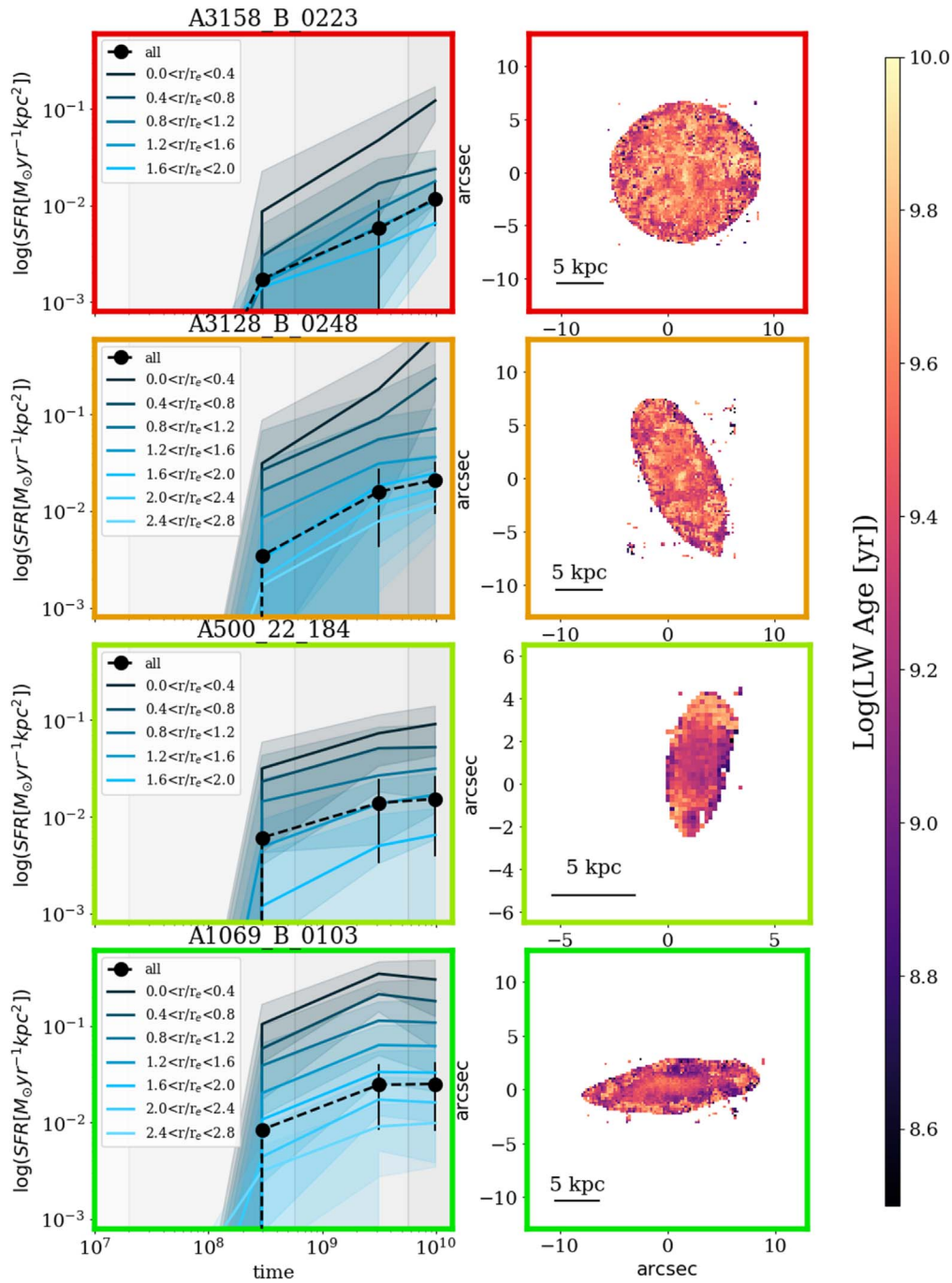


**Figure 10.** Left panels: SFHs in equally spaced different regions of four galaxies of the sample. The number of regions depends on the extension of the galaxy and are indicated in the label. The black dots and dashed lines represent the SFH of the galaxy across the entire galaxy disk. Shaded areas and black lines show the  $1\sigma$  dispersion of the curves. In the background, the gray areas identify the width of the bins. Right panels: maps of luminosity-weighted ages. Galaxies are surrounded by squares colored following the scheme of Figure 1. Galaxies are rainbow-colored by increasing  $EW(H\beta)$ , as measured on the integrated spectra (see Table 2).

concentrated Balmer line gradients in the central 1 kpc, even though we are hitting the regime where results are dominated by the Point-Spread Function. We note, however, that differently from the other studies, we could inspect the gradient out to large galactocentric distances.

A reason for the mixing results is that different studies are based on different techniques (long-slit spectroscopy versus IFU data), samples are very small (typically of the order of 10 galaxies at most), heterogeneous in terms of redshift range, environment, galactocentric distance probed, definition of PSB galaxies and have been hampered by physical scale resolution

constraints. Studies based on larger and more homogeneous samples and with higher spatial resolution would be necessary to firmly determine the gradients.

In the PSB galaxies, this young component is expected to be observable as a Balmer line absorption enhancement and gradient in the central region (Pracy et al. 2005; Snyder et al. 2011). Pracy et al. (2013) have analyzed four low-luminosity PSBs in different environments, including a cluster member and found that all four galaxies do have centrally concentrated gradients in the young stellar population contained within the central  $\sim 1$  kpc. In Figure 7, we have shown the  $H\beta$  gradients

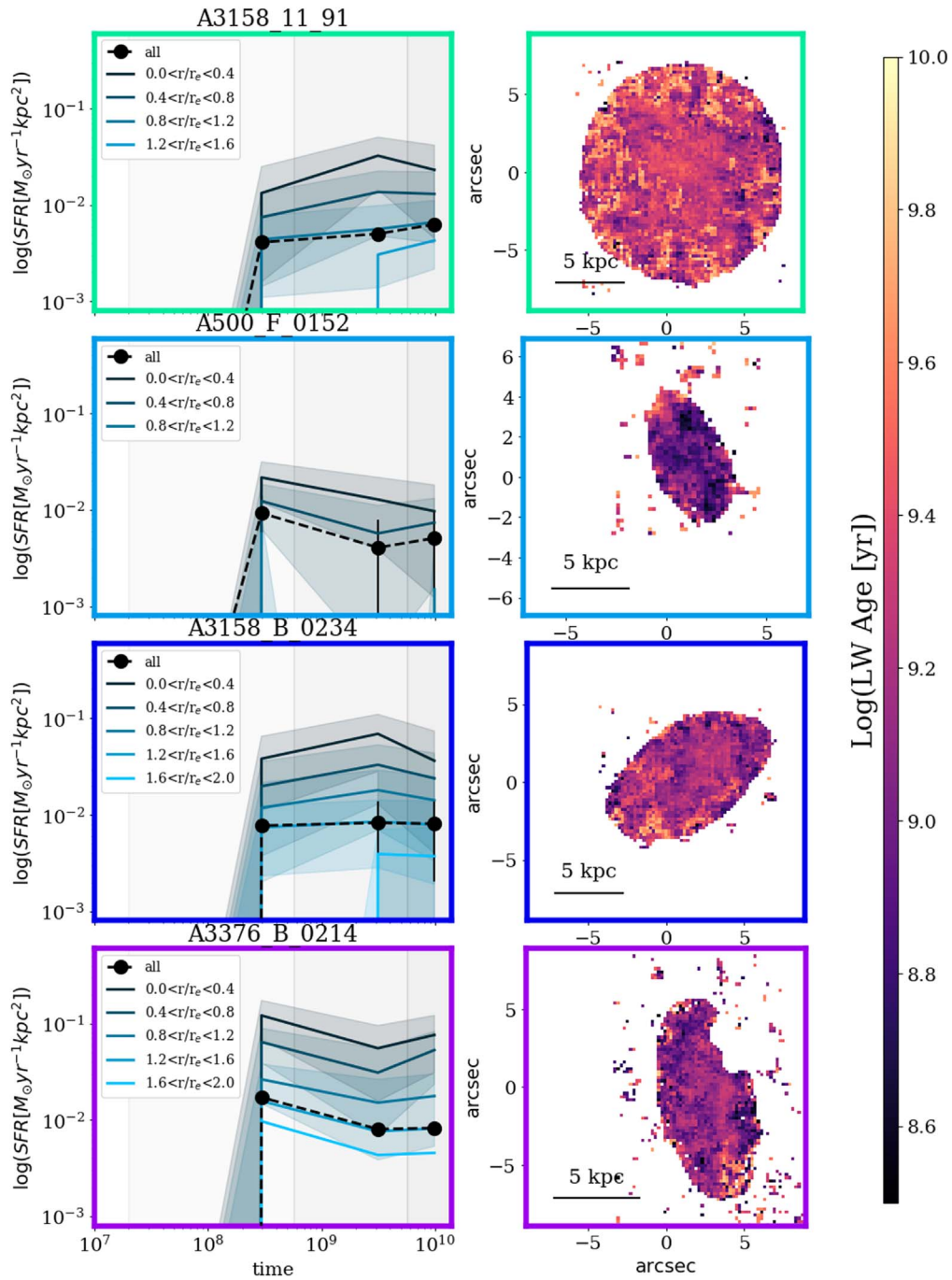


Figure 11. Same as Figure 10, but for the other four galaxies of the sample.

for our sample and highlighted the 1 kpc size for each galaxy separately. In agreement with the results presented by Pracy et al. (2013), the galaxies classified as  $k + a/a + k$  show hints of centrally concentrated Balmer line gradients in the central 1 kpc, even though we are hitting the regime where results are dominated by the point-spread function.

### 7.1. The Formation Scenario

As mentioned in Section 1, two main scenarios have been proposed to explain the formation of PSB galaxies. In the field, galaxy interaction and mergers are most likely the main mechanisms involved, while in clusters, ram pressure stripping

has been advocated. In the following, we will discuss the main observables that argue for or against the two scenarios for our sample galaxies.

#### 7.1.1. The Cluster Environment

The eight galaxies belong to five different clusters of the OMEGAWINGS survey. The main properties of the clusters are summarized in Table 4. Clusters are characterized by different values of velocity dispersion ( $550 < \sigma \text{ (km/s)} < 950$ ), suggesting that galaxies might feel cluster-specific processes with different strengths. A3376, A3158, and A3128 also belong to

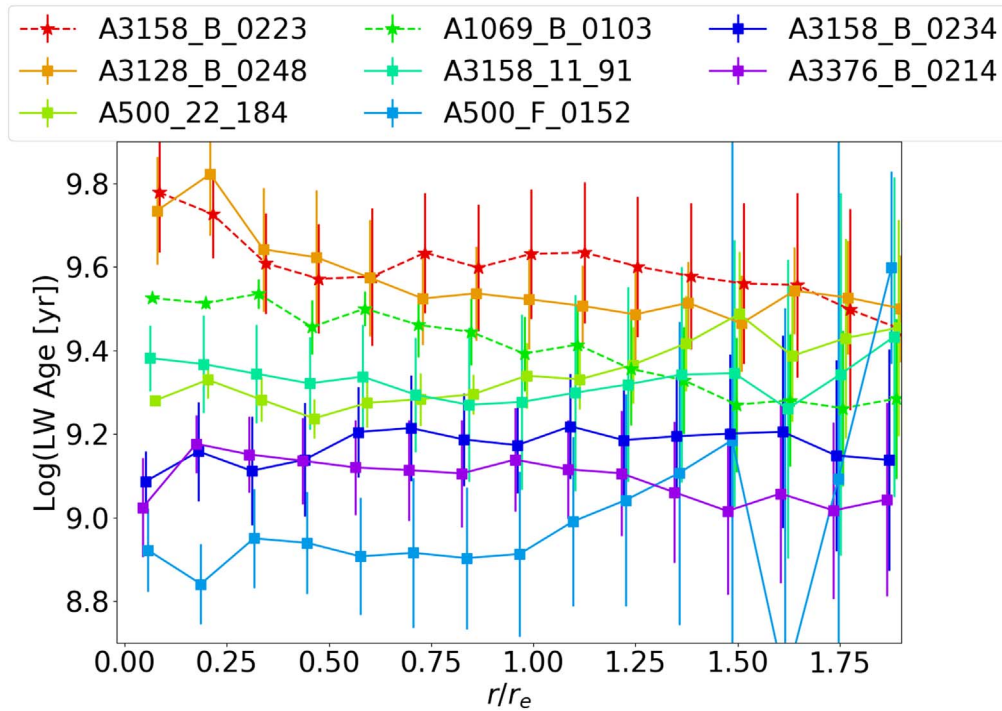


**Figure 12.** Luminosity-weighted age gradients in units of  $r_e$ , for each galaxy of the sample. Errors represent the standard deviation ( $1\sigma$ ). A small horizontal shift has been applied to the points for display purposes. Galaxies represented by stars have  $k$  integrated spectra, galaxies represented by squares have  $k + a/a + k$  integrated spectra.

**Table 3**

Pearson  $r$ -correlation Test Results Performed on the Luminosity-weighted Age Gradients

Id	Coefficient	$p$ -value
A500_22_184	0.85	6e-05
A500_F_0152	0.5	0.07
A3158_B_0234	0.39	0.1
A3376_B_0214	-0.6	0.01
A3376_B_0214*	0.2	0.6
A3158_11_91	-0.006	1
A3128_B_0248	-0.7	0.0006
A1069_B_0103	-0.96	6e-09
A3158_B_0223	-0.80	0.0003

**Note.** Values computed considering data within  $1 R_e$ , to better catch the dip in the galaxy center.

the Shapley superclusters, while A1069 and A500 are single, not merging systems.

Figure 13 presents the galaxy locations in the so-called projected phase-space diagram. This plot compares the projected distance from the cluster center and the line-of-sight velocity relative to the cluster velocity, normalized by the cluster size and velocity dispersion, respectively. Generally, galaxies at different positions in their orbit and with different times since infall occupy different regions in projected phase-space diagrams (Oman et al. 2013), which could be associated with different amounts of tidal mass-loss (Smith et al. 2015) and/or different strength of ram pressure stripping (Paper IX, Jaffé et al. 2015).

According to cosmological simulations (Haines et al. 2015; Rhee et al. 2017), galaxies that have been in a cluster for a very long time have lower velocities and clustercentric radii because

**Table 4**

Properties of the Clusters Hosting the PSBs: Cluster Name, Coordinates, Redshifts, Velocity Dispersions, and Virial Radius

Cluster	R.A. (J2000)	Decl. (J2000)	$z_{cl}$	$\sigma_{cl}$ (km s <sup>-1</sup> )	$R_{200}$ (Mpc)
A3376	90.1712	-40.0444	0.04652	756 <sup>+39</sup> <sub>-37</sub>	1.7 ± 0.2
A3158	55.71487	-53.62543	0.05947	948 <sup>+48</sup> <sub>-46</sub>	1.9 ± 0.1
A3128	52.4639	-52.5806	0.06033	793 <sup>+40</sup> <sub>-38</sub>	1.6 ± 0.2
A1069	159.9308	-8.6867	0.06528	542 <sup>+36</sup> <sub>-38</sub>	1.2 ± 0.2
A500	69.7187	-22.11	0.06802	660 <sup>+33</sup> <sub>-34</sub>	1.8 ± 0.2

**Note.** Values are from Moretti et al. (2017) and Biviano et al. (2017).

they have had enough time to sink into the potential well of the cluster. On the other hand, infalling galaxies approach the cluster core with high relative velocities at all clustercentric distances. Observations of galaxies in clusters confirm this scenario (Jaffé et al. 2015; Yoon et al. 2017).

All of our galaxies are located between 0.3 and  $1 R_{200}$ , therefore, avoiding the cluster cores, but they are characterized by quite large a range of relative velocities ( $0.2-2.8 |\Delta(v)|/\sigma$ ), indicating they are moving toward or away from their cluster centers with different speeds.

A3128\_B\_0248 is the galaxy with the highest relative velocity ( $|\Delta(v)|/\sigma = 2.8$ ), but it shows passive features. It might therefore be either a pre-processed galaxy or an ancient infaller, rather than a recent infaller. Rhee et al. (2017) have indeed shown that  $\sim 40\%$  of galaxies in this area are ancient contaminants to the recent infaller population. A500\_22\_184 and A3158\_B\_0234 are very close to the edge of the typical region delimited by the escape velocity in relaxed systems, and given their spectral properties, they are consistent with being recent infallers that suffer a truncation of the star formation as a

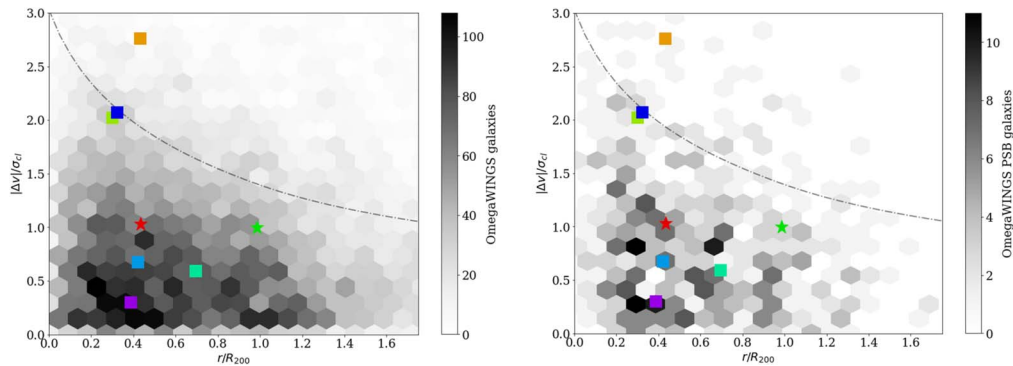


**Figure 13.** Location in projected position vs. velocity phase-space of the PSB galaxies analyzed in the paper. Galaxies represented by stars have  $k$  integrated spectra, galaxies represented by squares have  $k + a/a + k$  integrated spectra. The background shows the distribution of all OMEGAWINGS clusters with spectroscopic completeness  $>50$  per cent stacked together (left panel) and the distribution of OMEGAWINGS PSBs from Paccagnella et al. (2017) stacked together (right panel, green color bar). The gray curve corresponds to the 3D (un-projected) escape velocity in an NFW halo with concentration  $c = 6$  for reference.

consequence of their first encounter with the harsh cluster environment.

The other galaxies are located inside the typical trumpet-shaped region of the relaxed systems, in an area where both recent and ancient infallers could be actually found (Rhee et al. 2017).

We remind the reader that galaxies in A3376, A3158, and A3128 are part of the Shapley supercluster; therefore, their position in the phase space need to be treated with caution as cluster mergers can displace galaxy positions.

In Figure 13, galaxies are overplotted on the projected phase space diagram of all OMEGAWINGS galaxies (left panel) and on all of the OMEGAWINGS PSB galaxies from Paccagnella et al. (2017) (right panel). 2d  $k$ - $s$  tests state that the galaxies analyzed in this paper have a different distribution from the total population of cluster members, while it is indistinguishable from the entire PSB population. The position of most of them in the phase-space diagram is consistent with a recently infalled population that have been into clusters for at least one pericenter passage (i.e.,  $\geq 1$  Gyr). These galaxies could therefore be descendants of galaxies that quickly lost the gas when they were on first infall due to ram pressure stripping (i.e., jellyfish galaxies).

While the galaxies presented here have no star formation throughout the disk, GASP has been very successful in also identifying PSB regions in galaxies currently undergoing ram pressure stripping (Paper IV; Paper XXIII), highlighting how rapid events exhausting the gas due to ram pressure do produce PSB spectra.

### 7.1.2. Ruling Out Galaxy Mergers

The projected stellar angular momentum per unit mass,  $\lambda_R$  parameter (Emsellem et al. 2007, 2011), is commonly used to quantify the kinematic state of early-type galaxies. Emsellem et al. (2007) showed that galaxies can be separated into two distinct kinematic classes depending on the value of  $\lambda_R$ : the fast and slow rotators. Most of the early-type galaxies are classified as fast rotators (Emsellem et al. 2011), as also  $k + a/a + k$  galaxies (Pracy et al. 2009, 2012; Swinbank et al. 2012). The dearth of slow rotators in the  $E + A$  population has been used to argue against the need for major galaxy mergers in their production (Pracy et al. 2009, 2012), since the probability of a rotating remnant increases as the mass ratio of the progenitors involved in the merger increases (Bournaud et al. 2008) and

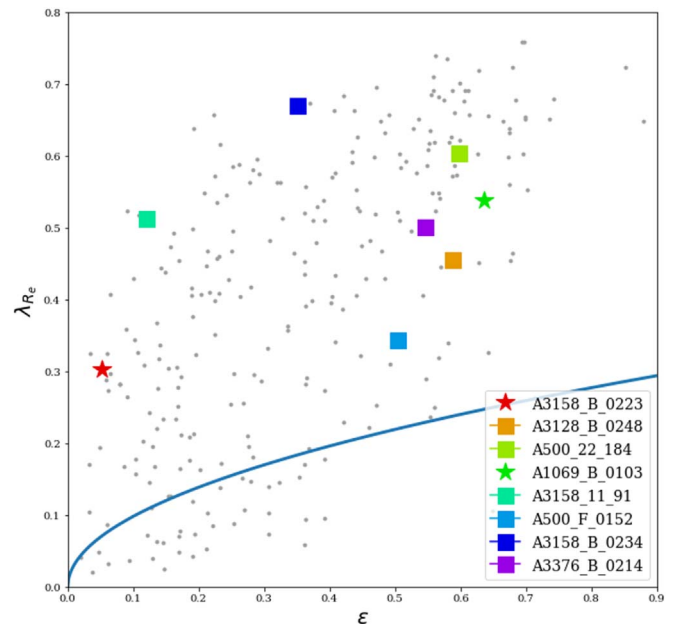


**Figure 14.**  $\lambda_{R_e}$  vs. the ellipticity  $\epsilon$  for the sample galaxies (red dots and squares) compared with ATLAS3D sample (gray dots, from Emsellem et al. 2011). Slow and fast rotators are split by the blue line.

major mergers should result in an increased fraction of slow rotators (see also Graham et al. 2019).

Figure 14 shows the  $\lambda_R$  parameter versus ellipticity for the sample. As reference, the data points of the 260 early-type galaxies in the nearby universe of ATLAS<sup>3D</sup> from Emsellem et al. (2011) are also shown. All of the galaxies are clearly fast rotators. This piece of evidence, together with the regular morphologies (Figure 2) and stellar kinematics (Figure 4) and the characterization of the environment, argue against the merger scenario.

In addition, we have also more carefully investigated the local environment of the eight galaxies, to look for signs for possible merger features. In particular, we checked whether (1) they have companions, (2) they are in substructures, and (3) they are in high-density regions.

We searched all of the OMEGAWINGS sample candidate companions with measured redshift and measured galaxy properties. Only in two cases we have found suitable candidates: A500\_22\_184, the least massive system in our

sample, has a massive ( $M_* = 7 \times 10^{10} M_\odot$ , a factor of  $200\times$  larger) passive galaxy at  $\sim 80$  kpc and with a velocity difference of  $\sim 135$  km s $^{-1}$ . A3158\_B\_0223, the most massive object in our sample, has a close companion at 40 kpc. The velocity difference between the two is  $\sim 135$  km s $^{-1}$ . The companion is also passive and has a similar stellar mass ( $M_* = 2.6 \times 10^{10} M_\odot$ ). The same galaxy is also the only galaxy that is most likely part of substructure in its cluster. Substructures have been defined running the DS+ method of Biviano et al. (2017) on the cluster members.

The projected local galaxy densities (LD) were derived calculating the number of galaxies per Mpc $^2$  (see Vulcani et al. 2012, for details), using the 10th nearest neighbors with  $M_V \leq -19.5$ . The galaxy local densities range between  $0.97 < \log(LD(\text{Mpc}^{-3})) < 1.5$ . As reference, the median project local density cluster members above  $3.5 \times 10^9 M_*/M_\odot$  (the OMEGAWINGS mass completeness limit) is  $1.2 \pm 0.2$ . Therefore, these galaxies are found in averagely dense regions and not in the most extreme ones.

These pieces of evidence also argue against the merger scenario.

## 8. Summary and Conclusions

GASP is a project developed to understand gas accretion and removal processes in the different environments, with the aim to determine the role of the environment in shaping galaxy properties.

In this paper, we have presented the characterization of eight galaxies, included in the GASP sample as representative of the final stage of the evolution of galaxies in clusters.

The combination of integrated and spatially resolved properties of the galaxies have allowed us to divide galaxies into three groups.

A3158\_B\_0234, A3376\_B\_0214, and A500\_F\_0152 are  $k + a/a + k$  galaxies: they are located in the blue region of the color–magnitude diagram, have  $\text{EW}(\text{H}\beta) > 2.8 \text{ \AA}$  both when considering the integrated spectrum and when considering stacked spectra representative of different portions of the galaxies. Their LWA are  $< 10^{9.2}$  yr at all galactocentric distances, their SFH show signs of a rapid truncation. A500\_F\_0152 and A3376\_B\_0214 also show hint of a central SF enhancement just before quenching, while A3158\_B\_0234 does not. The galaxies are located in almost the same region of the projected phase space diagram: relatively low velocities ( $< 1 |\Delta(v)|/\sigma$ ), intermediate clustercentric distances, where relatively recent infallers can be found (Rhee et al. 2017).

A3158\_B\_0223 and A3128\_B\_0248 are very red, have  $k$  spectra at all distances from the center and declining SFH since  $10^{10}$  yr ago. They show the oldest luminosity-weighted ages ( $> 10^{9.6}$  yr). All of their properties indicate they have been fully quenched more than 1 Gyr ago. Given their stellar mass, these galaxies (as also A1069\_B\_0103) might have been quenched while still in the field, or in pre-processing groups.

The remaining three galaxies have properties intermediate between the aforementioned groups, with intermediate colors, intermediate LWA, intermediate EW ( $\text{H}\beta$ ), and less steeply declining SFH. Of these, A500\_22\_184 stands out, because even though it has an overall quite low global EW( $\text{H}\beta$ ), it has a very steep  $\text{H}\beta$  gradient, suggesting the presence of a central burst. The galaxy cannot be conclusively classified as  $a + k/k + a$  because

the truncation of the star formation in the outer disk regions occurred more than  $10^9$  yr ago, but the central regions still show  $a + k/k + a$  signatures.

The three groups are probably not distinct classes, but represent an evolutionary sequence cluster galaxies can undergo: after entering the cluster environment, galaxies abruptly quench as an effect of gas removal due to ram pressure stripping. At first, these objects maintain their morphology and blue colors, but their spectral properties immediately change: emission lines disappear and deep absorption lines emerge. If a burst of star formation occurred prior to quenching, absorption lines are even deeper and EW gradients are visible. As time goes by, galaxy populations age and become older, EW of absorption lines decrease, and as a consequence, galaxy colors become redder. After  $> 10^9$  yr, EW of absorption lines are minimal and galaxies are red. All of these changes occur before the galaxy morphology changes, suggesting that morphological transformations occur on even longer timescales. Nonetheless, morphological transformations can occur, as witnessed by the presence of S0s in our sample. These observations support a scenario in which at least some S0s can form via ram pressure stripping (and perhaps additional mechanisms) in clusters.

Most of the galaxies have been quenched outside-in, i.e., the outskirts reached undetectable SFRs before the inner regions, even though this feature is more visible for the  $k$  galaxies (see Figure 9).

The outside-in quenching, the lack of signs of interactions and the high  $\lambda_R$  measured, together with the fact that the galaxies are found in dense clusters, point to a scenario according to which ram pressure stripping has removed the gas.

It is interesting to observe that actually ram pressure stripping can produce a variety of spatial trends in SFH during quenching.

While in this paper, we have focused only on the optical properties of the galaxies, to get a complete understanding of the baryonic cycle in PSB galaxies, a multi-tracer study covering atomic, molecular, and ionized gas, would be very important, similarly to what was performed in Klitsch et al. (2017) for field galaxies. This would quantify the state and distribution of all of the gas components and predict whether these galaxies still have a substantial reservoir of atomic and/or diffuse molecular gas, which could eventually form stars again.

We thank the referee for their comments that helped to improve the manuscript. Based on observations collected at the European Organisation for Astronomical Research in the Southern Hemisphere under ESO program 196.B-0578. This project has received funding from the European Research Council (ERC) under the Horizon 2020 research and innovation program (grant agreement No. 833824). We acknowledge funding from the INAF PRIN-SKA 2017 program 1.05.01.88.04 (PI: Hunt). We acknowledge financial contribution from the contract ASI-INAF n.2017-14-H.0, from the grant PRIN MIUR 2017 n.20173ML3WW\_001 (PI Cimatti) and from the INAF mainstream funding program (PI Vulcani). Y.J. acknowledges support from CONICYT PAI (Concurso Nacional de Inserción en la Academia 2017) No. 79170132 and FONDECYT Iniciación 2018 No. 11180558.

Facility: VLT(MUSE).

## Appendix Surface Brightness Profiles

As explained in detail in A. Franchetto et al. (2020, in preparation), we perform an isophotal analysis on the *I*-band images using the ELLIPSE task in IRAF (Jedrzejewski 1987) to extract the Surface Brightness profiles (SBPs) of the galaxies. ELLIPSE fits on the image a series of elliptical isophotes such to minimize the deviations from the real shape of the galaxy isophotes. Then it returns the mean intensity along the ellipse, semimajor axis, position angle and ellipticity ( $\epsilon$ ) for each one. We mask out foreground stars, nearby and background galaxies, bad pixels, and bright spots before fitting the isophotes.

In order to investigate the photometric structures that contribute to the galaxy light distribution, we carry out a parametric monodimensional decomposition of the observed SBPs.

The components and the corresponding photometric laws considered to perform the best-fit decomposition are as follows:

$$\text{Bulge: } I(r) = I_e 10^{-b_n[(r/r_e)^{1/n}-1]} \quad (2)$$

(Sérsic 1968), where  $r_e$ ,  $I_e$ , and  $n$  are the effective radius of the bulge, the intensity at  $r_e$ , and the index parameter, respectively, while  $b_n$  is a linear function of  $n$  (Caon et al. 1993, Equation (6));

$$\text{Disk: } I(r) = I_0 e^{-(r/r_d)} \quad (3)$$

(Freeman 1970), where  $I_0$  and  $r_d$  are the central intensity and the scale parameter of the disk;

$$\text{Broken disk:} \\ I(r) = \begin{cases} I_{0,1} e^{-(r/r_{d,1})} & r < r_{br} \\ I_{0,2} e^{-(r/r_{d,2})} & r > r_{br} \end{cases} \quad (4)$$

(Pohlen et al. 2002), where the two equations represent the inner and the outer behavior of the disk SBP, both described by an exponential law with different scale parameters ( $r_{d,1}$ ,  $r_{d,2}$ ) and central intensities ( $I_{0,1}$ ,  $I_{0,2}$ ). The break radius  $r_{br}$  sets the change of the slope

$$\text{Cut - off disk: } I(r) = I_0 e^{-(r/r_d)-(r_c/r)^3} \quad (5)$$

(Kormendy 1977), where the exponential disk is characterized by an inner drop for radii lower than the cutoff radius  $r_c$ ;

$$\text{Lens: } I(r) = I_{0,1} [1 - (r/r_1)^2] \quad (6)$$

(Duval & Athanassoula 1983), where  $I_{0,1}$  and  $r_1$  are the central intensity and the size of the lens, respectively;

$$\text{Bar: } I(r) = I_{0,b} [1 - (r/a_b)^2]^{(n_b+0.5)} \quad (7)$$

(Ferrers 1877), where  $I_{0,b}$ ,  $a_b$ , and  $n_b$  are the central intensity, the size of the lens, and the strength parameter of the bar, respectively.

Based on the visual inspection of the *I* band images and the extracted SBPs, for each galaxy, we define a photometric model as the sum of the observed components. The best values of their free parameters are derived using the Python software package LMFIT (Newville et al. 2014) that implements a nonlinear least-squares minimization of the  $\chi^2$

$$\chi^2 = \sum_i \frac{[I_{\text{obs},i} - I_{\text{mod},i}(\mathbf{p})]^2}{w_i^2}, \quad (8)$$

where  $\mathbf{p}$  is the set of variables in the model  $I_{\text{mod}}$  and  $I_{\text{obs}}$  is the observed SBP. The fitting of the data points is achieved using a

**Table 5**

AIC Statistics for the Adopted Multicomponent Fit ( $\text{AIC}_{\text{multi}}$ ) and for a Basic Bulge+Disk Decomposition  $\text{AIC}_{b+d}$

Id	$\text{AIC}_{\text{multi}}$	$\text{AIC}_{b+d}$
A500_22_184	-183.23	-112.39
A500_F_0152	-129.17	-121.22
A3158_B_0234	-127.69	-36.65
A3376_B_0214	-75.65	43.11
A3158_11_91	-241.64	-182.57
A3128_B_0248	-107.84	-107.84
A1069_B_0103	40.03	56.61
A3158_B_0223	-98.11	-49.93

weighting factor  $w_i$  that takes into account the errors of the isophote intensities and the fraction of the masked pixels along the isophotes. Moreover, to reduce the seeing effect that levels off the central intensity, we exclude the inner points within  $0''.5$ .

To test the quality of the fits, we have applied the Akaike information criterion (AIC; Akaike 1973), which is an estimator that gives the relative quality of statistical models for a given set of data. Given a set of candidate models for the data, the preferred model is the one with the minimum AIC value. Thus, AIC rewards the goodness of a fit, but it also includes a penalty that is an increasing function of the number of estimated parameters. The penalty discourages overfitting, because increasing the number of parameters in the model almost always improves the goodness of the fit. We compare the AIC results of our decompositions to those obtained by performing a simple bulge+disk decomposition. As shown in Table 5, the AIC value is always larger in the case of the bulge+disk decomposition, reassuring us about the choice of the model. We note that A3128\_B\_0248 is the only galaxy for which no third component exists. Similar results are obtained also using the Bayesian information criterion (BIC).

## ORCID iDs

Benedetta Vulcani  <https://orcid.org/0000-0003-0980-1499>  
 Jacopo Fritz  <https://orcid.org/0000-0002-7042-1965>  
 Bianca M. Poggianti  <https://orcid.org/0000-0001-8751-8360>  
 Daniela Bettoni  <https://orcid.org/0000-0002-4158-6496>  
 Andrea Franchetto  <https://orcid.org/0000-0001-9575-331X>  
 Alessia Moretti  <https://orcid.org/0000-0002-1688-482X>  
 Marco Gullieuszik  <https://orcid.org/0000-0002-7296-9780>  
 Yara Jaffé  <https://orcid.org/0000-0003-2150-1130>  
 Andrea Biviano  <https://orcid.org/0000-0002-0857-0732>

## References

- Alatalo, K., Cales, S. L., Rich, J. A., et al. 2016, *ApJS*, 224, 38  
 Akaike, H. 1973, in Proc. of the 2nd International Symposium on Information Theory, ed. B. N. Petrov & F. Csáki (Budapest: Akadémiai Kiadó), 267  
 Baldwin, J. A., Phillips, M. M., & Terlevich, R. 1981, *PASP*, 93, 5  
 Balogh, M., Navarro, J., & Morris, S. 2000, *ApJ*, 540, 113  
 Balogh, M. L., Baldry, I. K., Nichol, R., et al. 2004, *ApJL*, 615, L101  
 Barro, G., Faber, S. M., Pérez-González, P. G., et al. 2014, *ApJ*, 791, 52  
 Bekki, K. 1999, *ApJL*, 510, L15  
 Bekki, K. 2009, *MNRAS*, 399, 2221  
 Bekki, K. 2014, *MNRAS*, 438, 444  
 Bekki, K., Couch, W. J., & Shioya, Y. 2002, *ApJ*, 577, 651  
 Bekki, K., Couch, W. J., Shioya, Y., & Vazdekis, A. 2005, *MNRAS*, 359, 949  
 Bellhouse, C., Jaffé, Y., Hau, G., et al. 2017, *ApJ*, 844, 49

- Bellhouse, C., Jaffe, Y. L., McGee, S. L., et al. 2019, *MNRAS*, **485**, 1157
- Biviano, A., Moretti, A., Paccagnella, A., et al. 2017, *A&A*, **607**, A81
- Blake, C., Pracy, M. B., Couch, W. J., et al. 2004, *MNRAS*, **355**, 713
- Boselli, A., Boissier, S., & Cortese, L. 2006, *ApJ*, **651**, 811
- Boselli, A., Cortese, L., Boquien, M., et al. 2014, *A&A*, **564**, A67
- Boselli, A., & Gavazzi, G. 2006, *PASP*, **118**, 517
- Boselli, A., Roehlly, Y., Fossati, M., et al. 2016, *A&A*, **596**, A11
- Bournaud, F., Duc, P.-A., & Emsellem, E. 2008, *MNRAS*, **389**, L8
- Bressan, A., Marigo, P., Girardi, L., et al. 2012, *MNRAS*, **427**, 127
- Bryant, J. J., Owers, M. S., Robotham, A. S. G., et al. 2015, *MNRAS*, **447**, 2857
- Bundy, K., Bershady, M. A., Law, D. R., et al. 2015, *ApJ*, **798**, 7
- Byrd, G., & Valtonen, M. 1990, *ApJ*, **350**, 89
- Caldwell, N., Whipple, F. L., Rose, J. A., Franx, M., & Leonardi, A. J. 1996, *AJ*, **111**, 78
- Caon, N., Capaccioli, M., & D'Onofrio, M. 1993, *MNRAS*, **265**, 1013
- Cappellari, M., & Copin, Y. 2003, *MNRAS*, **342**, 345
- Cappellari, M., & Emsellem, E. 2004, *PASP*, **116**, 138
- Cardelli, J. A., Clayton, G. C., & Mathis, J. S. 1989, *ApJ*, **345**, 245
- Chabrier, G. 2003, *PASP*, **115**, 763
- Chen, Y.-M., Shi, Y., Wild, V., et al. 2019, *MNRAS*, **489**, 5709
- Chilingarian, I. V., De Rijcke, S., & Buyle, P. 2009, *ApJL*, **697**, L111
- Couch, W. J., & Sharples, R. M. 1987, *MNRAS*, **229**, 423
- Davis, T. A., van de Voort, F., Rowlands, K., et al. 2019, *MNRAS*, **484**, 2447
- De Lucia, G., Weinmann, S., Poggianti, B. M., Aragón-Salamanca, A., & Zaritsky, D. 2012, *MNRAS*, **423**, 1277
- Dressler, A., & Gunn, J. E. 1982, *ApJ*, **263**, 533
- Dressler, A., & Gunn, J. E. 1983, *ApJ*, **270**, 7
- Dressler, A., & Gunn, J. E. 1992, *ApJS*, **78**, 1
- Duval, M. F., & Athanassoula, E. 1983, *A&A*, **121**, 297
- Elmegreen, B. G., & Parravano, A. 1994, *ApJ*, **435**, L121
- Emsellem, E., Cappellari, M., Krajnović, D., et al. 2007, *MNRAS*, **379**, 401
- Emsellem, E., Cappellari, M., Krajnović, D., et al. 2011, *MNRAS*, **414**, 888
- Fasano, G., Vanzella, E., Dressler, A., et al. 2012, *MNRAS*, **420**, 926
- Ferland, G. J., Porter, R. L., van Hoof, P. A. M., et al. 2013, *RMxAA*, **49**, 137
- Ferrers, N. M. 1877, *QJPM*, **14**, 1
- Fossati, M., Mendel, J. T., Boselli, A., et al. 2018, *A&A*, **614**, A57
- Freeman, K. C. 1970, *ApJ*, **160**, 811
- French, K. D., Arcavi, I., & Zabludoff, A. 2016, *ApJL*, **818**, L21
- French, K. D., Yang, Y., Zabludoff, A., et al. 2015, *ApJ*, **801**, 1
- Fritz, J., Moretti, A., Gullieuszik, M., et al. 2017, *ApJ*, **848**, 132
- Fritz, J., Poggianti, B. M., Bettoni, D., et al. 2007, *A&A*, **470**, 137
- Fritz, J., Poggianti, B. M., Cava, A., et al. 2011, *A&A*, **526**, A45
- George, K., Poggianti, B., Gullieuszik, M., et al. 2018, *MNRAS*, **479**, 4126
- George, K., Poggianti, B. M., Bellhouse, C., et al. 2019, *MNRAS*, **487**, 3102
- Ghigna, S., Moore, B., Governato, F., et al. 1998, *MNRAS*, **300**, 146
- Gladders, M. D., Oemler, A., Dressler, A., et al. 2013, *ApJ*, **770**, 64
- González-Martín, O., Masegosa, J., Márquez, I., Guainazzi, M., & Jiménez-Bailón, E. 2009, *A&A*, **506**, 1107
- González-Martín, O., Masegosa, J., Márquez, I., Guerrero, M. A., & Dultzin-Hacyan, D. 2006, *A&A*, **460**, 45
- Goto, T. 2005, *MNRAS*, **357**, 937
- Graham, M. T., Cappellari, M., Bershady, M. A., & Drory, N. 2019, [arXiv:1911.06103](https://arxiv.org/abs/1911.06103)
- Gullieuszik, M., Poggianti, B., Fasano, G., et al. 2015, *A&A*, **581**, 41
- Gullieuszik, M., Poggianti, B., Moretti, A., et al. 2017, *ApJ*, **846**, 27
- Gunn, J. E., & Gott, J. R. 1972, *ApJ*, **176**, 1
- Haines, C. P., Finoguenov, A., Smith, G. P., et al. 2018, *MNRAS*, **477**, 4931
- Haines, C. P., Pereira, M. J., Smith, G. P., et al. 2015, *ApJ*, **806**, 101
- Head, J. T. C. G., Lucey, J. R., & Hudson, M. J. 2015, *MNRAS*, **453**, 3730
- Hopkins, P. F., Cox, T. J., Dutta, S. N., et al. 2009, *ApJS*, **181**, 135
- Hopkins, P. F., Hernquist, L., Cox, T. J., et al. 2006, *ApJS*, **163**, 1
- Jaffé, Y., Poggianti, B., Moretti, A., et al. 2018, *MNRAS*, **476**, 4753
- Jaffé, Y. L., Smith, R., Candlish, G. N., et al. 2015, *MNRAS*, **448**, 1715
- Jedrzejski, R. I. 1987, *MNRAS*, **226**, 747
- Klitsch, A., Zwaan, M. A., Kuntschner, H., et al. 2017, *A&A*, **600**, 80
- Kormendy, J. 1977, *ApJ*, **217**, 406
- Kronberger, T., Kapferer, W., Ferrari, C., Unterguggenberger, S., & Schindler, S. 2008, *A&A*, **481**, 337
- Larson, R. B., Tinsley, B. M., & Caldwell, C. N. 1980, *ApJ*, **237**, 692
- Lee, B., Chung, A., Tonnesen, S., et al. 2017, *MNRAS*, **466**, 1382
- Martin, D. C., Wyder, T. K., Schiminovich, D., et al. 2007, *ApJS*, **173**, 342
- Martínez-Serrano, F. J., Serna, A., Doménech-Moral, M., & Domínguez-Tenreiro, R. 2009, *ApJ*, **705**, L133
- McGee, S. L., Balogh, M. L., Bower, R. G., Font, A. S., & McCarthy, I. G. 2009, *MNRAS*, **400**, 937
- Moore, B., Katz, N., Lake, G., Dressler, A., & Oemler, A. 1996, *Natur*, **379**, 613
- Moretti, A., Gullieuszik, M., Poggianti, B., et al. 2017, *A&A*, **599**, 81
- Moretti, A., Poggianti, B. M., Gullieuszik, M., et al. 2018, *MNRAS*, **475**, 4055
- Newville, M., Stensitzki, T., Allen, D. B., & Ingargiola, A. 2014, LMFFIT: Non-Linear Least-square Minimization and Curve-Fitting for Python, Zenodo, doi:10.5281/zenodo.11813
- Norton, S. A., Gebhardt, K., Zabludoff, A. I., & Zaritsky, D. 2001, *ApJ*, **557**, 150
- Nulsen, P. E. J. 1982, *MNRAS*, **198**, 1007
- Oman, K. A., Hudson, M. J., & Behroozi, P. S. 2013, *MNRAS*, **431**, 2307
- Owers, M. S., Hudson, M. J., Oman, K. A., et al. 2019, *ApJ*, **873**, 52
- Paccagnella, A., Vulcani, B., Poggianti, B. M., et al. 2017, *ApJ*, **838**, 148
- Paccagnella, A., Vulcani, B., Poggianti, B. M., et al. 2019, *MNRAS*, **482**, 881
- Pattarakijwanich, P., Strauss, M. A., Ho, S., & Ross, N. P. 2016, *ApJ*, **833**, 19
- Pawlik, M. M., McAlpine, S., Trayford, J. W., et al. 2019, *NatAs*, **3**, 440
- Poggianti, B. M., Aragón-Salamanca, A., Zaritsky, D., et al. 2009, *ApJ*, **693**, 112
- Poggianti, B. M., Ignesti, A., Gitti, M., et al. 2019, GASP XXIII: A Jellyfish Galaxy as an Astrophysical Laboratory of the Baryonic Cycle, Tech. Rep., <https://www.eso.org/public/news/eso1725/>
- Poggianti, B. M., Moretti, A., Gullieuszik, M., et al. 2017, *ApJ*, **844**, 48
- Poggianti, B. M., Smail, I., Dressler, A., et al. 1999, *ApJ*, **518**, 576
- Pohlen, M., Dettmar, R. J., Lütticke, R., & Aronica, G. 2002, *A&A*, **392**, 807
- Pracy, M. B., Couch, W. J., Blake, C., et al. 2005, *MNRAS*, **35**, 1421
- Pracy, M. B., Croom, S., Sadler, E., et al. 2013, *MNRAS*, **432**, 3131
- Pracy, M. B., Kuntschner, H., Couch, W. J., et al. 2009, *MNRAS*, **396**, 1349
- Pracy, M. B., Owers, M. S., Couch, W. J., et al. 2012, *MNRAS*, **420**, 2232
- Rhee, J., Smith, R., Choi, H., et al. 2017, *ApJ*, **843**, 128
- Roche, N., Humphrey, A., Gomes, J. M., et al. 2015, *MNRAS*, **453**, 2350
- Roediger, E., & Brüggem, M. 2006, *MNRAS*, **369**, 567
- Rowlands, K., Heckman, T., Wild, V., et al. 2018, *MNRAS*, **480**, 2544
- Rowlands, K., Wild, V., Nesvadba, N., et al. 2015, *MNRAS*, **448**, 258
- Sánchez, A. G., Baugh, C. M., Percival, W. J., et al. 2006, *MNRAS*, **366**, 189
- Sanders, D. B., Soifer, B. T., Elias, J. H., et al. 1988, *ApJ*, **325**, 74
- Schawinski, K., Urry, C. M., Simmons, B. D., et al. 2014, *MNRAS*, **440**, 889
- Sérsic, J. 1968, Atlas de Galaxias Australes (Cordoba, Argentina: Observatorio Astronomico)
- Smith, R., Sánchez-Janssen, R., Beasley, M. A., et al. 2015, *MNRAS*, **454**, 2502
- Snyder, G. F., Hopkins, P. F., & Hernquist, L. 2011, *ApJL*, **728**, L24
- Socolovsky, M., Almaini, O., Hatch, N. A., et al. 2018, *MNRAS*, **476**, 1242
- Swinbank, A. M., Balogh, M. L., Bower, R. G., et al. 2012, *MNRAS*, **420**, 672
- Tran, K. H., Franx, M., Illingworth, G., Kelson, D. D., & van Dokkum, P. 2003, *ApJ*, **599**, 865
- Tran, K. H., Franx, M., Illingworth, G. D., et al. 2004, *ApJ*, **609**, 683
- Tran, K. H., Franx, M., Illingworth, G. D., et al. 2007, *ApJ*, **661**, 750
- Vulcani, B., Poggianti, B., Jaffé, Y., et al. 2018a, *MNRAS*, **480**, 3152
- Vulcani, B., Poggianti, B. M., Fasano, G., et al. 2012, *MNRAS*, **420**, 1481
- Vulcani, B., Poggianti, B. M., Fritz, J., et al. 2015, *ApJ*, **798**, 52
- Vulcani, B., Poggianti, B. M., Gullieuszik, M., et al. 2018b, *ApJL*, **866**, L25
- Vulcani, B., Poggianti, B. M., Moretti, A., et al. 2019, *MNRAS*, **488**, 1597
- Wong, O. I., Schawinski, K., Kaviraj, S., et al. 2012, *MNRAS*, **420**, 1684
- Wu, P.-F., Gal, R. R., Lemaux, B. C., et al. 2014, *ApJ*, **792**, 16
- Yagi, M., & Goto, T. 2006, *AJ*, **131**, 2050
- Yang, X., Mo, H. J., & van den Bosch, F. C. 2008, *ApJ*, **676**, 248
- Yang, Y., Zabludoff, A. I., Zaritsky, D., Lauer, T. R., & Mihos, J. C. 2004, *ApJ*, **607**, 258
- Yesuf, H. M., Faber, S. M., Trump, J. R., et al. 2014, *ApJ*, **792**, 84
- Yoon, H., Chung, A., Smith, R., & Jaffé, Y. L. 2017, *ApJ*, **838**, 81
- Zabludoff, A. I., Zaritsky, D., Lin, H., et al. 1996, *ApJ*, **466**, 104
- Zwaan, M. A., Kuntschner, H., Pracy, M. B., & Couch, W. J. 2013, *MNRAS*, **432**, 492